Renewable Energy 219 (2023) 119519

Contents lists available at ScienceDirect

Renewable Energy

journal homepage: www.elsevier.com/locate/renene

Aero-structural rapid screening of new design concepts for offshore wind turbines

Alejandra S. Escalera Mendoza [a,*], D. Todd Griffith [a], Michael Jeong [b], Chris Qin [b], Eric Loth [b], Mandar Phadnis [c], Lucy Pao [c], Michael S. Selig [d]

[a] Department of Mechanical Engineering, The University of Texas at Dallas, Richardson, TX, USA
[b] Department of Mechanical and Aerospace Engineering, University of Virginia, Charlottesville, VA, USA
[c] Department of Electrical, Computer, and Energy Engineering, University of Colorado Boulder, Boulder, CO, USA
[d] Department of Aerospace Engineering, University of Illinois at Urbana-Champaign, Urbana, IL, USA

ARTICLE INFO

Keywords:
Aero-structural design
Structural optimization
Offshore wind turbine
Load alignment
Downwind rotor
Levelized cost of energy

ABSTRACT

The development of large-scale wind turbines is challenged by loads, mass, and cost growth, and more flexible blades that impact power and tower clearance. Further, the long-duration design iterations with standard-sequential-multidisciplinary processes challenge the development of new timely and robust designs. To overcome these limitations and answer open questions of large-scale wind turbines, we develop and demonstrate an aero-structural rapid screening (ASRS) design approach. ASRS uses optimization techniques, emulates a baseline controller, produces detailed blade, tower, and monopile models, and provides fast aerodynamic, structural, and economic results. Blade deflection is introduced as a design variable to achieve load-aligned designs as a function of wind speed for passive load alleviation. To illustrate the approach, a large set of 25 MW rotors for offshore and fixed-bottom wind turbines are studied for variations in blade pre-cone, load alignment via blade deflection, and upwind vs. downwind configurations. These designs vary in number of blades, blade length, axial induction factor, and airfoil family. We demonstrate that blade deflection can be designed to maximize energy capture and minimize turbine mass. ASRS is demonstrated to identify trends and trade-offs that are useful to down-select to options to be studied further using aero-servo-elastic simulations with high-fidelity control design.

1. Introduction

Global wind power capacity is growing to meet the increasing renewable energy demands to reduce carbon emissions and dependence on fossil fuels. Larger wind turbines provide more power due to the increase in rotor swept area and access to higher wind speeds at taller hub heights. However, the need for rapid development of large-scale wind turbines is challenged by the mass growth of turbine components, increase in loads due to higher wind speeds leading to either stiff and heavy blades or very flexible structures that are difficult to control, and long duration between design iterations that may limit exploration of system level trade-offs and integration of innovations in standard sequential multi-disciplinary processes. Studies of novel concepts and design approaches help reduce risks and enable larger turbines. Some of these concepts include downwind turbines in two and three-bladed and low and maximum axial induction factor configurations actively studied in the Segmented Ultra-light Morphing Rotor (SUMR) project for 25 MW offshore and fixed-bottom turbines [1,2], which is the next leap in power rating. SUMR design studies performed on two-bladed downwind 13 MW, 25 MW, and 50 MW turbines [3–7] show the benefit of applying innovative design approaches to reduce mass, cost, and overall levelized cost of energy (LCOE). To ensure LCOE is minimized on a system-wide and accurate basis, it is important to investigate system level trade-offs and reduce the time between design iterations to integrate innovations into the wind turbine design process such as two-bladed, downwind, and passive load alleviation that result in robust designs comparable to conventional design configurations, which is the focus of this study.

1.1. Design and optimization of wind turbines review

The aforementioned challenges have led to the development of design approaches that consider various strategies for design iterations (e.g., sequential and integrated/simultaneous), number of concentration areas considered in one iteration, number of variables studied,

* Corresponding author.
E-mail addresses: ase180001@utdallas.edu (A.S. Escalera Mendoza), tgriffith@utdallas.edu (D.T. Griffith).

https://doi.org/10.1016/j.renene.2023.119519
Received 8 April 2023; Received in revised form 20 October 2023; Accepted 24 October 2023
Available online 25 October 2023

and use of advanced tools and techniques (e.g., optimization). Efforts to optimize the blade structure individually are shown by Maki et al. [8] and Bottasso et al. [9]. Maki et al. [8] evaluated 1.3–1.9 MW three-bladed horizontal axis wind turbines (HAWTs) with a multi-level optimization. The competing objectives of annual energy production (AEP) and blade root bending moment were evaluated in the lower level, and the cost of energy (system-level objective) was minimized in the upper level. However, Maki et al. [8] concluded the blade structure has a small influence on the LCOE. On the other hand, Bottasso et al. [9] applied a multi-level approach for the structural optimization of blades (with prescribed aerodynamic shape) of a 2 MW wind turbine rotor. Optimizations were performed at a coarse level (1D beam model and 2D cross-sectional model) and then at the fine level (3D finite element model or FEM) to facilitate the process and reduce computational resources.

However, Deshmukh and Allison [10] stated that co-design is essential for producing more meaningful solutions and considered aero-servo-elastic interactions in a multidisciplinary optimization of the blades. The objective of their study was to maximize AEP while varying the external geometry of the blade and analyzing structural constraints (blade stress, strain, and frequencies and tower-base stress). Deshmukh and Allison [10] showed an AEP increase of 8% and indicated strong interdependence between plant and control design. Zalkind et al. [11] examined the effect of rotor design choices on AEP and the structural loads on major wind turbine components (tower, hub, main bearing, and yaw bearing) by using a harmonic model for structural loading derived from FAST simulations. They designed 42 different rotors to explore reductions in cost of energy and analyzed the effect on tower design and closed-loop control for upwind and downwind configurations. Bortolotti et al. [12] performed sequential aerodynamic-structural optimizations to study trade-offs in the wind turbine rotor design process for 3–6 MW onshore turbines. The blade outer shape was optimized first to maximize the power coefficient, then the spar cap and trailing edge reinforcement were sized to minimize the mass using a gradient-based approach. The loads applied were calculated using a surrogate model that applies polynomial tuning to loads obtained at rated conditions to reconstruct the critical design load case (DLC). The surrogate model reduces the extensive computation time that would otherwise be required if optimizations were to be performed with all relevant DLCs.

The tower was also studied separately from the blade. Malaawi [13] worked extensively on the tower design optimization of a 100 kW HAWT and explored various objective functions (mass reduction, stiffness maximization, stiffness-to-mass ratio maximization, and maximization of tower natural frequencies) using Powell's multi-dimensional search technique and Euler–Bernoulli theory for beam deflection. Negm and Maalawi [14] expanded the work and concluded that the frequency and mass of the tower are continuous functions. They indicated that the first natural frequency of the tower or tower with rotor assembly can be fixed at any desired value, and other variables can be optimized to meet that frequency. Further optimization methods for the tower were developed by Horvath and Toth [15] who combined FEM and computational fluid dynamic (CFD) methods to explore tower cross-sections and heights, Yoshida [16] employed genetic algorithms to optimize the tower using cans and variable thickness walls, Uys et al. [17] utilized a direct search method for a model with conical steel shell segments stiffened with rings, and Al-Sanad et al. [18] applied a genetic algorithm with reliability-based design to obtain 15.1% mass reduction and indicated that tower design is driven by fatigue reliability.

In recent years there has been more interest to investigate multi-objective and multi-disciplinary methods to gain better understanding of the coupling effects between wind turbine components to obtain more efficient designs. Ashuri et al. [19] applied a multidisciplinary and multi-level design optimization to minimize LCOE of the NREL 5 MW HAWT [20] by simultaneously optimizing the aerodynamic and structural design of the rotor and the tower that led to a LCOE reduction of 2.3%. The authors state that LCOE is a continuous and smooth function that couples aerodynamics and structures; thus, gradient-based optimization can be used with a multi-start approach. Ning et al. [21] studied the effect of optimization settings on the solution and corresponding limitations. The authors state that sequential aero-structural optimizations lead to sub-optimal results and recommended to include a cost analysis because percent differences in mass and cost can be different. Ning et al. [21] used SQL fmincon gradient, central difference, and multi-start to find the global optimum and analyzed different objective functions. The authors concluded that minimizing the cost of energy (COE) is the best to balance aerodynamic and structural performance while including costs, and that only optimizing the rotor (and not the tower) leads to over emphasizing the rotor. The authors also pointed out that solutions may be subject to the fidelity of the cost and physics models.

Additional system-level design studies and optimization were performed by Bortolotti et al. [22]. The authors utilized a multi-disciplinary procedure (including the tower and rotor) that is "preliminary-detailed" because it sizes the overall machine (rotor diameter, tower height) while accounting for the aero-servo-elastic couplings. The objective is COE minimization and significant improvements are obtained compared to baseline 2.2 MW onshore and 10 MW offshore turbines. The authors conclude that low induction rotors are not competitive against high-efficiency rotors. Zhu et al. [23] investigated the coupling effects of a 1.5 MW turbine between blade and tower using optimizations with conflicting objectives: maximize AEP and minimize wind turbine mass. A 16.06% AEP increase and 10.6% mass decrease was obtained with a genetic algorithm optimization. Zhu et al. [23] stated that only few works that couple the effects of the rotor and tower are available due to the complexities in modeling and simulating the interaction between them. However, large computational resources and/or long simulation times are often required by optimizations with a large number of variables, higher fidelity models, and with integrated/simultaneous strategies.

1.2. Upwind vs. Downwind wind turbines review

Downwind designs have also been considered because the blades deflect away from the tower instead of towards the tower; thus, the tower clearance constraint becomes inactive or less active. The most common HAWTs are upwind. Downwind wind turbines were not favored due to their higher aero-acoustic emissions and fatigue loads because the blades pass through the tower wake (tower shadow effect). However, Simpson et al. [24] show that for load-aligned downwind 13 MW designs the tower shadow effect was weaker compared to turbulent loads and did not significantly increase blade root bending moments. Furthermore, Loth et al. [25] found that such 13 MW load-aligned downwind designs do not lead to significant acoustic problems since the combination of coning and high flexibility avoids the "thumping" noise effect that was observed in previous stiff downwind rotors. Therefore, the growing size of turbines has led to an interest in downwind wind turbines because they allow relaxing the blade tip deflection constraint to prevent tower strike as illustrated in Fig. 1.

Frau et al. [26] performed unsteady and 3D CFD simulations of a 2 MW HAWT in downwind and upwind configurations. The authors used similar operating conditions for both configurations and observed that the downwind configuration has increases of 3% in power, 3% in thrust, and 14% in blade loads. These changes are attributed to higher flow incidences along the blade span and axial velocity on the inboard portion of the blade span. Despite the increase in thrust and blade loads, Frau et al. [26] concluded that downwind wind turbines are better suited for the growing offshore wind market.

Ning and Petch [27] studied downwind vs. upwind concepts on land-based turbines of 5–7 MW range, 105–175 rotor diameter, and different wind speed sites using optimization with 90% exact gradients.

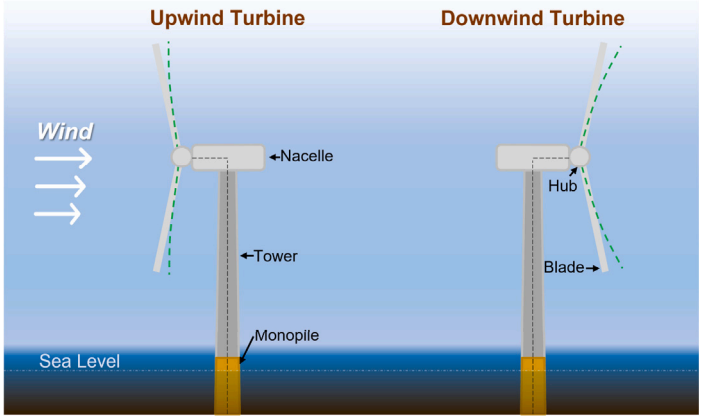

Fig. 1. Illustration of upwind and downwind offshore fixed-bottom two-bladed wind turbines with undeflected (gray) and deflected blades (dashed green).

The authors state benefits of downwind turbines because upwind designs require stiff blades to meet the tower-strike constraint, which becomes more critical as blade size/power rating continues to grow. Ning and Petch [27] concluded that downwind wind turbines offer little benefit in high wind speed sites (tower mass increases although blade mass decreases), but they show 1%–2% decrease in cost of energy in low wind speed sites (where blade mass is more significant). They recommend further study to understand the dynamic effects of flexible downwind blades.

Larwood and Chow [28] performed experimental studies using the NREL Phase VI wind turbine in downwind and upwind configurations. They observed no power reduction for the downwind configuration except near rated power and attributed this to "inboard three-dimensional effects". Larwood and Chow [28] showed that downwind wind turbines have lower average flap bending loads (due to the downwind coning), but blade fatigue loads were increased due to the tower shadow. These were mitigated using a tower shroud (fairing) that must remained aligned to the free-stream to work effectively. Wang et al. [29] performed an experimental study of upwind and downwind configurations of a 280 mm rotor diameter wind turbine. They also concluded that downwind wind turbines have higher fatigue loads due to tower shadow, but observed a 2.3% decrease in power.

Bortolotti et al. [30,31] performed a study of 10 MW upwind and downwind HAWTs. They obtained a blade mass reduction of 4.4% for the downwind option, but with 1.2% AEP loss and 0.9% LCOE increase due to the smaller capture area of downwind blades. Bortolotti et al. [31] stated that ideal uptilt and coning values are not defined, and suggested areas of further research such as advanced downwind rotor controls, novel comparisons based on higher fidelity aerodynamic models, and full system optimization with offshore floating platforms.

The design of downwind wind turbines for multi-megawatt machines has been studied in the segmented ultra-light morphing rotor (SUMR) project. Loth et al. [32] proposed the concept of load alignment (i.e., active blade coning) in which the blades can change its pre-cone angle depending on the wind condition (incorporating a behavior similar to palm trees in high wind or hurricane conditions). However, the active coning mechanism would need to handle high loads and was considered too expensive. Nonetheless, significant research has been performed on 13–50 MW wind turbines to study the design and trade-offs of extreme-scale wind turbines [4,6,33,34], and a small-scale demonstrator of the SUMR 13 MW turbine design was built and tested in the National Wind Technology Center (NWTC) [25,35,36]. Research is still ongoing on 25 MW turbines [1,5].

1.3. Objective and organization of this work

Few academic studies have been performed that couple the effects of rotor and tower design choices. More studies are required to evaluate trade-offs of downwind design and low-axial induction factor rotor designs. To the knowledge of the authors of this work, no academic studies were performed to investigate blade flexibility as a passive load alleviation strategy and evaluate the effect of different airfoil families on the turbine performance and design. Additionally, minimizing gravitational loads (equivalent to the mass growth) of larger wind turbines while meeting design requirements is a challenge [6,34], and further exploration of trade-offs among design variables is needed.

In this work, an aero-structural rapid screening (ASRS) design approach is developed to answer open research questions and address challenges of large-scale wind turbines with emphasis on offshore and fixed-bottom designs. ASRS is a conceptual-level design approach that includes fast and detailed evaluations (aerodynamics, structures, and cost) of wind turbine designs (rotor, tower, and monopile) using optimization techniques and by emulating a baseline controller to produce design loads. The present study demonstrates ASRS on a wide range of pre-defined aerodynamic rotor designs that must achieve 25 MW of power rating and that vary in blade length, axial induction factor, airfoil family, and number of blades. The study of these design variables adds new information to the body of research that shines light on trade-offs important for large-scale wind turbines. By pre-defining the aerodynamic rotor designs there is more freedom to explore a wide range of variables that would otherwise take extensive computational resources and be challenging for optimization algorithms. The ASRS approach introduces the blade deflection/passive cone as a new design variable for passive load alleviation via load-alignment, and it is used to obtain more accurate estimates of load and energy captured at the conceptual-level design. A first analysis of blade pre-cone and passive cone is performed for downwind and upwind configurations to quantify trade-offs related to structural performance, mass, cost, AEP, and LCOE for 25 MW turbines, and to evaluate the benefit of lower risk of tower strike for downwind designs.

The paper is organized as follows. First, the ASRS design approach is described in detail. Second, a summary of the wide range of aerodynamic designs evaluated in this work is presented and justified. Third, a validation of ASRS with aero-servo-elastic simulations is shown. Fourth, results are presented for three case studies: (1) blade pre-cone vs. passive load alleviation via blade deflection for a single aerodynamic rotor design, (2) rapid screening of 25 different downwind aerodynamic rotor designs, and (3) an upwind versus downwind analysis for a single aerodynamic rotor design. Finally, conclusions and future research options are summarized.

2. Methodology: Introduction to Aero-Structural Rapid Screening (ASRS)

Aero-structural rapid screening (ASRS) is a design approach for fast and detailed evaluation (aerodynamics, structures, and cost) of

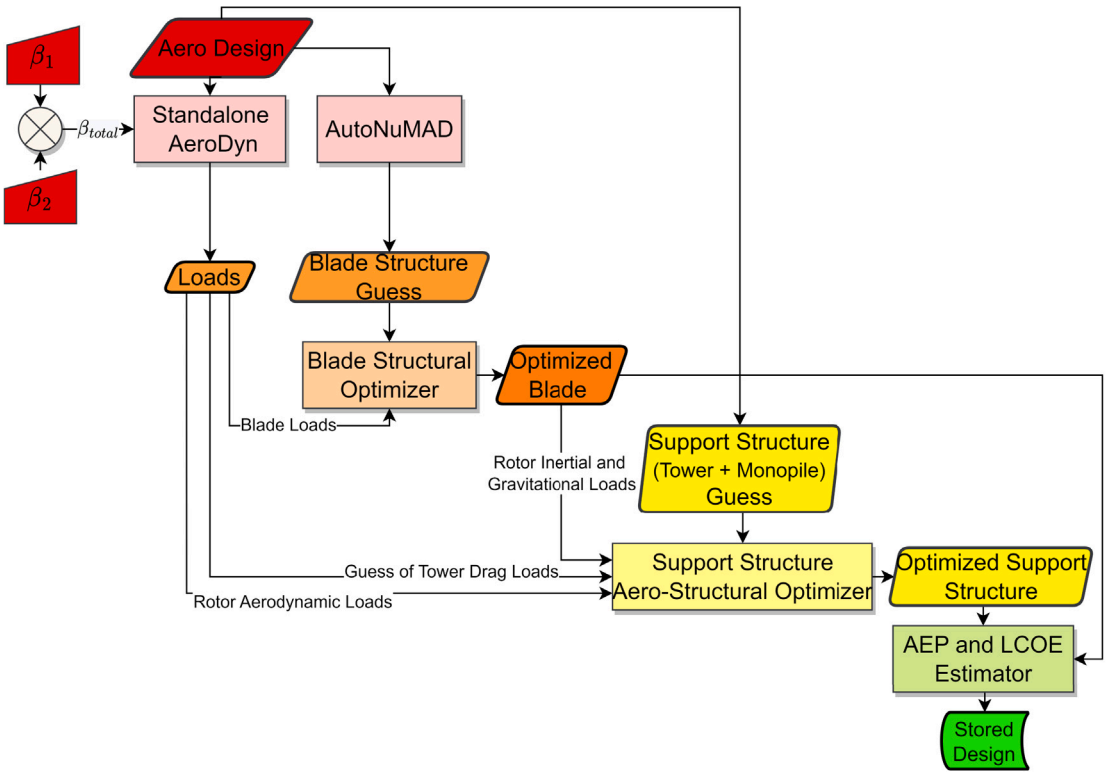

Fig. 2. ASRS approach with four color coded levels: Level 1 is red, Level 2 is orange, Level 3 is yellow, and Level 4 is green.

wind turbine designs using optimization techniques and by emulating a baseline controller. Fig. 2 illustrates the ASRS approach that includes detailed models for the design of the blade, tower, and monopile, and consists of four levels in which these are evaluated and optimized. In Level 1, rotor loads at rated wind speed are obtained with an aerodynamic analysis. In Level 2, a blade structural optimization is performed using the loads from Level 1. In Level 3, an aero-structural optimization is performed to design the support structure (tower and monopile). The wind turbine AEP and LCOE is evaluated in Level 4. The support structure design follows the blade design because the rotor thrust and overturning moment greatly impact the tower design [1], but the tower does not affect the rotor design as significantly. Downwind turbines have blades passing through the wake of tower (tower shadow) may see a higher effect on the blade fatigue life compared to upwind turbines, but the tower shadow effect may be weaker compared to turbulent loads and not significantly increase blade root bending moments [24]. Tower shadow and fatigue analysis require higher fidelity analysis with turbulence which are beyond the scope of the ASRS approach that focuses on the rapid and detailed design space exploration. However, results obtained with ASRS can be used as a baseline to perform aero-servo-elastic analyses including fatigue and tower shadow. The following sub-sections describe in detail each of these steps.

2.1. Aerodynamic analysis

In Level 1 shown in Fig. 2, the aerodynamic performance of a pre-defined rotor aerodynamic design is evaluated using steady wind and including wind shear with the standalone version of AeroDyn 15 (AD15) [37,38]. The ASRS approach emulates a baseline controller in steady wind by assuming constant tip-speed-ratio (TSR or ratio of the speed of the blade tip to the free-stream wind speed) and blade pitch in below-rated operation (Region 2), and that maximum thrust occurs at rated wind speed (because the blade-pitch controller would engage in above-rated operation, Region 3, to regulate power and loads). By pre-defining the rotor aerodynamic characteristics the aerodynamic

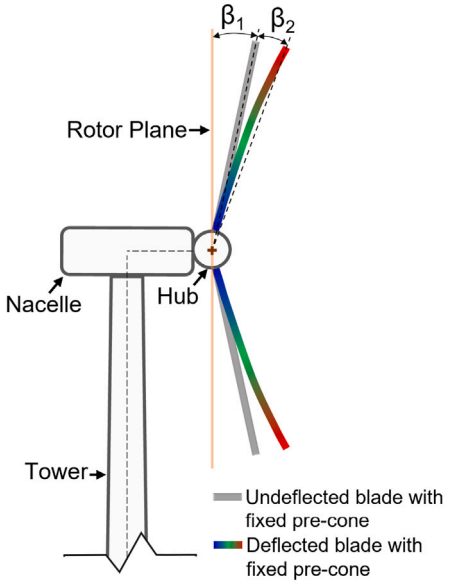

Fig. 3. ASRS definition of β_1 and β_2 for an example downwind turbine.

designer has more freedom to explore the design space, and it also reduces the time between full design iterations since optimizations over a wide range of combined aerodynamic and structural variables would be challenging for optimization algorithms.

The standalone AD15 calculates the aerodynamic performance assuming rigid blades; however, the blade deflection can significantly impact the aerodynamic performance. Thus, it is helpful to account for it in early design stages. In this work, we show an approach to account

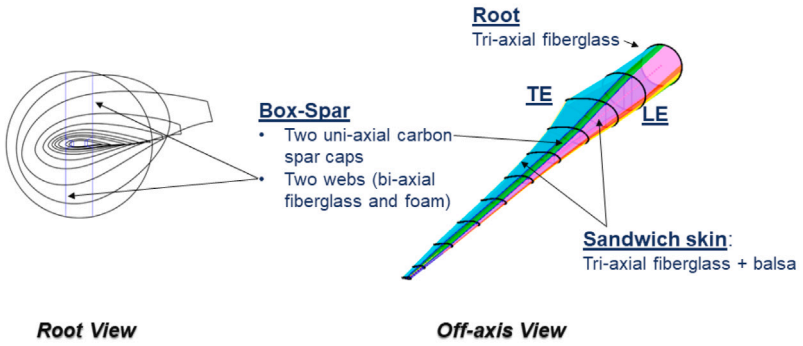

Fig. 4. Example blade model generated with AutoNuMAD.

for the blade deflection without creating a full aero-servo-elastic model that requires a tuned controller. The blade deflection is accounted by assuming the pre-cone angle in the AD15 driver input file to be equal to β_{total} that is the summation of the fixed blade pre-cone β_1 and passive cone angle β_2 as shown in Eq. (1). The latter (β_2) is the angle equivalent to the blade out-of-plane (OoP) deflection defined in Eq. (2) (where "L" is the blade length), and is used as means for passive load alleviation via load alignment. Fig. 3 illustrates that β_2 provides passive load alleviation by reducing the rotor swept area (similar to blade pre-cone). By pre-defining the blade deflection at rated wind speed in steady wind ($\beta_{2_{rated}}$), the effect of both the actual blade pre-cone and the tip deflection are accounted that provide better estimates of the rated wind speed and aerodynamic loads. The aerodynamic loads obtained in Level 1 are the distributed flapwise and edgewise aerodynamic blade forces, rotor forces and moments at the hub, and tower drag loads (for an initial guess of the tower geometry).

$$\text{Total Cone Angle}(\beta_{total}) = \text{Pre-cone}(\beta_1) + \text{Passive Cone}(\beta_2) \tag{1}$$

$$\beta_2(\text{deg}) = \arcsin\left(\frac{OoP}{L}\right) \tag{2}$$

2.2. Blade structural optimization

The blade outer geometry and a well-informed guess of its internal structure (detailed composite layups) are defined with AutoNuMAD [3,34,39–41] which is a semi-automated tool based on the NuMAD framework [42]. Fig. 4 shows an example blade created with AutoNuMAD.

In Level 2 of ASRS, the layup of the blade spar caps is optimized to minimize blade cost and meet the tip deflection and blade strength design requirements, which typically are the first main two blade design requirements. In ASRS, the blade must achieve a tip flapwise deflection equivalent to $\beta_{2_{rated}}$ with aerodynamic loads at steady wind and rated wind speed, and meet strain requirements using extreme loads. The extreme loads are bending moments obtained by multiplying the blade aerodynamic loads at rated wind speed (from ASRS Level 1) with tuning coefficients from the surrogate model presented in Bortolotti et al. [12]. The surrogate model is insensitive to the planform design and was obtained from simulation results of operational and storm DLCs that include gravitational and centrifugal effects. The structural optimization of the blade is performed with the settings listed below:

- Minimize $f(x)$ = *Blade Material Cost/Cost reference value* subject to:
    1. Upper deflection limit: *Blade deflection/deflection limit - (1+Upper Tolerance)* ≤ 0. Where the deflection limit is equivalent to $\beta_{2_{rated}}$.
    2. Lower deflection limit: *(1-Lower Tolerance) - Blade deflection/deflection limit* ≤ 0.
    3. Spar cap strain: *-Margin of Safety* ≤ 0. The strain is calculated using the extreme loads obtained with the surrogate model.
- Upper and lower bounds on six variables capture variations in the spar cap shape illustrated in Fig. 5 and are tabulated (as fractions of the reference values) in Table 1. The bound and reference values were selected based on careful evaluation of the blade optimization algorithm's performance and examination of manual 25 MW blade design results.

Table 1
Bounds for spar cap optimization variables.

No.	Description	Lower bound	Upper bound	Reference value
1	Location of point 2	0.03	0.15	Blade length
2	Location of point 3	0.17	0.54	Blade length
3	Location of point 4	0.55	0.95	Blade length
4	Layers at point 2 (foot)	0	1	230
5	Layers at points 3 & 4 (top)	0.34	1	440
6	Layers at point 5 (tip)	0.04	1	80

The cost function, nonlinear constraints, and the bounds are normalized to facilitate convergence and reduce the optimization time. Normalizing is a good and standard practice in optimization. The cost function was selected because it effectively captures the changes in the blade mass and quantifies the difference in cost of the various materials in the blade. The blade deflection is constrained with two nonlinear inequality constraints that represent an upper and lower bound of the tip deflection. This approach was selected because it facilitates convergence and reduces computation time by allowing tolerances in the tip deflection. The deflection tolerance is set to small values (+5 mm/–50 mm normalized by the deflection limit) to assure the analysis is in accordance with the assumptions in ASRS Level 1.

The third nonlinear constraint (the spar cap strain margin of safety or MS) is calculated with Eq. (3) where ε_U is the ultimate strength of the spar cap material. The safety factor (SF) is 2.977 that corresponds to an ultimate limit state analysis for composites as described in Griffith and Ashwill [43] and follows international design standards for blade design [44]. The strain is calculated at the center point of the spar cap for both the lower and upper pressure shells along the span of the blade, but only the minimum MS value is used in the nonlinear constraint equation.

$$MS = \frac{\varepsilon_U}{SF * Strain_{spar}} - 1 \tag{3}$$

PreComp [45] is used in the NuMAD framework to generate blade sectional structural properties that are used to calculate strain and deflection. Strain can be evaluated at any point on the cross-section of the blade as shown in Eq. (4) with edgewise stiffness (EI_{xx}), flapwise stiffness (EI_{yy}), edgewise bending moment (M_x), and flapwise bending

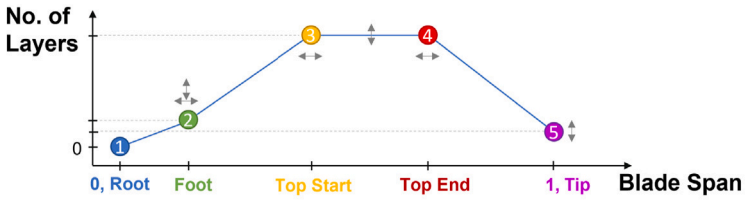

Fig. 5. Variables of spar cap layup (six gray arrows) used in the blade structural optimization.

moment (M_y). The sectional properties generated by PreComp are also used to calculate the blade deflection using a finite element tool based on an Euler–Bernoulli twelve degree-of-freedom (DOF) model coded in MATLAB [46]. The FEM tool is based on the work performed by Lopez [47], but was modified in this work to account for varying sectional properties along the blade length. The x and y terms represent the distances from the neutral axis to the point of interest in the cross-section. All components of Eq. (4) are transformed to a global coordinate system prior to calculating strains.

$$\epsilon(x,y) = \frac{M_x}{EI_{xx}} * y + \frac{M_y}{EI_{yy}} * x \tag{4}$$

In this work, the blade structural optimization is focused on the spar cap design that is driven by the aerodynamic-flapwise bending moments. All structural optimizations are performed with gradient based and nonlinear programming solver "fmincon" with the algorithm sequential quadratic programming "sqp" of MATLAB. Gradient-based optimization with a multi-start approach is used to find the global minima for the blade structural optimization because it requires less computational resources, the cost and constraint functions are continuous, and sufficient constraints are defined.

2.3. Tower and monopile aero-structural optimization

After the blade structure is optimized, the tower and monopile geometry and structure (diameter and wall thickness at the base and top assuming linear interpolation between the two) are optimized in Level 3 of ASRS. The tower and monopile optimization is performed with the procedure and assumptions described in Escalera Mendoza et al. [1] that also uses a gradient-based method to optimize the structure using continuous and analytical equations. The aero-structural optimization of the tower and monopile includes the tower aerodynamic drag loads and an additional constraint that requires 30% blade-to-tower clearance (more relevant for upwind designs) under normal operating conditions [44,48].

2.4. AEP and LCOE estimation

In ASRS Level 1, the rated wind speed is estimated by assuming a constant β_{total}. However, β_{total} is not constant because the blade deflection (β_2) increases with higher wind speed. The change of β_2 versus wind speed is denominated as a passive load alleviation profile and it is determined through consecutive iterations. The iteration process begins with calculating β_2 with the ASRS Level 1 loads at different wind speeds (every 2 m/s from V_{in} to V_{out}), then the newly found β_2 values are used to obtain new loads for the corrected β_{total} at each wind speed. The AEP is determined on each iteration and the iterations stop when the change in AEP (current iteration compared to last iteration) is approximately zero. The accuracy of the calculated AEP is demonstrated in the validation section. The AEP is an input for the LCOE model described next.

The LCOE is calculated with an explicit LCOE model for fixed-bottom offshore wind turbines by Qin et al. [2] that is based on the equivalent mass method by proposed by Garcia-Sanz [49]. This model presents a simplified framework where approximate cost coefficients (relative to component masses) are used to obtain a rapid estimate of LCOE with acceptable accuracy compared to the Wind-plant Integrated System Design and Engineering Model (WISDEM) [50], which is developed by NREL and includes a set of highly detailed and complex models for assessing overall wind turbine system cost. Furthermore, this explicit model includes updated material prices as well as operational and balance of station costs from recently published works [51,52] that reflect the latest developments in the wind energy industry. Thus, the explicit LCOE model is appropriate for the work performed herein.

Table 2
Cost factors of LCOE explicit framework.

Component	Baseline material	f_m	f_i	c_t ($/kg)
Blade	GFRP	1.7	0.1	2.08
	CFRP	1.7	0.1	16.44
Hub	Cast iron and steel	12.12	0.1	1.2
Nacelle	Cast iron and steel	3.5	0.1	1.54
Tower	Hot-rolled coil steel	1	0.1	1.2

$$LCOE = \frac{(CapEx + BOS) * FCR + OpEx}{AEP * (1 - AWL)} \tag{5}$$

Eq. (5) shows the LCOE calculation where the balance of station (BOS) is $1785/kW, the fixed charge rate (FCR) is 5.6%, and operational expenditures (OpEx) is $110/kW, which are values obtained directly from Stehly and Duffy [52]. The average wake losses (AWL) is assumed to be 15% (common estimation of wind farm effects). The capital expenditures (CapEx) is the summation of the CapEx estimation of individual components j obtained with Eq. (6) in which the mass m of the component is multiplied by the corresponding cost coefficient in Table 2 that includes material c_t, manufacturing f_m, and installation f_i cost coefficients. The material cost coefficient varies for each blade design because it is a function of the percent of fiberglass and carbon fiber reinforced plastics in the blade mass (GFRP and CFRP, respectively). More detailed descriptions of the explicit LCOE framework and an analysis for offshore turbines of 5–15 MW rating is provided in Qin et al. [2].

$$CapEx_j = m_j * (1 + f_{m,j} + f_{i,j}) * c_{t,j} \tag{6}$$

2.5. Material properties

Table 3 contains the material properties used in the structural components optimized herein. The tower and monopile are made of steel. The blade root is made of tri-axial fiberglass and the blade spar cap has uni-axial carbon fiber pre-preg.

3. Summary of aerodynamic designs

Aero-structural rapid screening is performed on the pre-defined aerodynamic designs shown in Fig. 6. Low axial-induction factor designs (a = 1/4) have lower thrust coefficients and reduce the aerodynamic loads on the blades (which may reduce mass and cost), but have the penalty of also having a lower power coefficient (which may reduce the total AEP). Thus, studying trade-offs of low axial-induction

Table 3
Material properties assumed for the blade, tower and monopile structural optimizations (E = Young's modulus, G = shear modulus, ν = Poisson's ratio, ρ = density, UTS = ultimate tensile strength, and YS = yield strength).

Material	E_{11} (GPa)	E_{22} (GPa)	G_{12} (GPa)	ν_{12}	ρ (kg/m^3)	UTS (MPa)	YS (MPa)
Tri-axial Fiberglass	24.9	15.4	8.3	0.376	1902.6	466.9	NA
Uni-axial Carbon Fiber	114.1	9.9	4.1	0.3	1525.5	1370	NA
Steel	210	210	80.8	0.3	8500	420	350

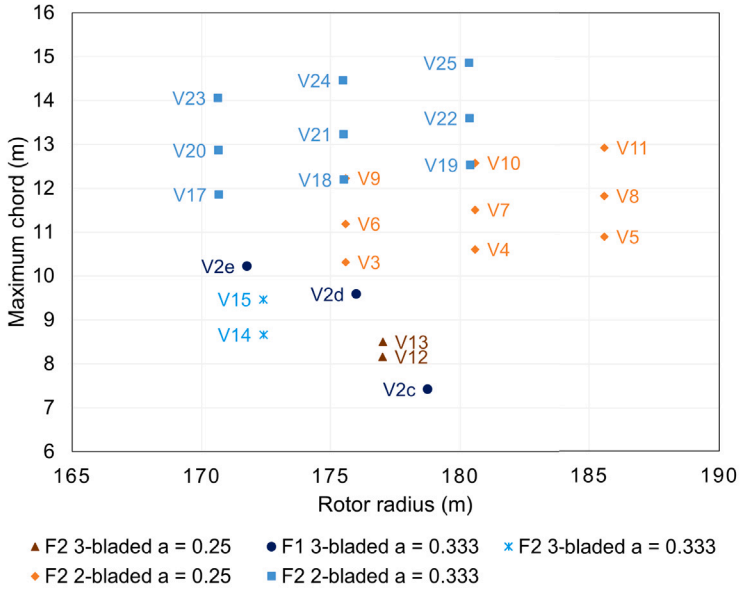

Fig. 6. Aerodynamic designs of 25 MW rated power studied with ASRS that differ in axial-induction factor (a = 0.25 and 1/3), blade length, chord size, number of blades (two and three–bladed), and airfoil family (F1 and F2 airfoil families).

factor designs are of interest in this work. Designs with axial-induction factor of a = 1/3 are the most common in the industry, these designs have higher thrust coefficients than low axial-induction factor designs, but also have higher power coefficients. In general, the low axial-induction factor designs shown in Fig. 6 have a larger rotor radius and smaller maximum chord than high axial-induction designs to achieve the same rated power of 25 MW. For both axial-induction factors (low and high/typical), two and three-bladed designs were created. Two-bladed designs have larger chords and thereby have similar rotor solidity compared to three-bladed designs (which have one more blade and thus do not need larger chords). Designs that have the same blade length but different maximum chord were obtained by varying the lift coefficient (C_l). Higher C_l distributions across the entire blade span result in lower chord values because there is an inverse relationship between C_l and chord for a fixed rated power. Designs with the F2 airfoil family overall result in designs with lower thickness-to-chord ratio compared to designs with the F1 airfoil family which were first presented by Ananda et al. [53].

4. ASRS validation with aero-servo-elastic simulations

Before using ASRS to examine a range of designs, the ASRS results for the V2e design are compared to outputs from higher fidelity aero-servo-elastic simulations. This validation provides confidence in the ASRS outputs and helps understand its limitations. The aero-servo-elastic simulations are performed using a baseline controller tuned for V2e. The baseline controller for V2e has two primary objectives based on the operating region. In below-rated operation (Region 2), the control objective is to maximize the power produced by V2e from the wind. The turbine is operated close to its maximum power coefficient $C_{p,max}$ to achieve this. The power coefficient C_p for a turbine is defined as the ratio of the power captured by the turbine to the power available in the wind (Pao and Johnson [54]). It is typically mapped as a function of the blade pitch angle and the TSR in a two-dimensional "C_p surface" plot. For operating near $C_{p,max}$ across Region 2, the blades are fixed at their optimal pitch angle, $\theta_{finepitch}$ for maximizing aerodynamic torque on the rotor and the generator torque, τ_g is varied to maintain the optimal TSR, λ_{opt}, by using the nonlinear control law [54]

$$\tau_g = K_{opt}\omega_g^2, \tag{7}$$

where ω_g is the generator speed and the optimal gain, K_{opt}, is calculated using the turbine parameters.

In above-rated operation (Region 3), the control objective is to regulate the power output to the rated capacity of the turbine for constraining structural loads and safe operation. In Region 3, the generator torque is saturated to its rated value, the generator speed is regulated by pitching the turbine blades to manipulate the aerodynamic torque on the rotor using a gain-scheduled proportional-integral (PI) controller

$$\theta = K_p(\theta)\omega_{err} + K_I(\theta)\int \omega_{err}dt, \tag{8}$$

where ω_{err} is the difference between the rated generator speed ω_{rated} and instantaneous generator speed ω_g, K_p and K_I are the PI gains scheduled per the instantaneous blade pitch angle θ. The gain scheduling is necessary for PI gains because the sensitivity of power to blade pitch varies across Region 3 [20]. The PI gains are tuned using an

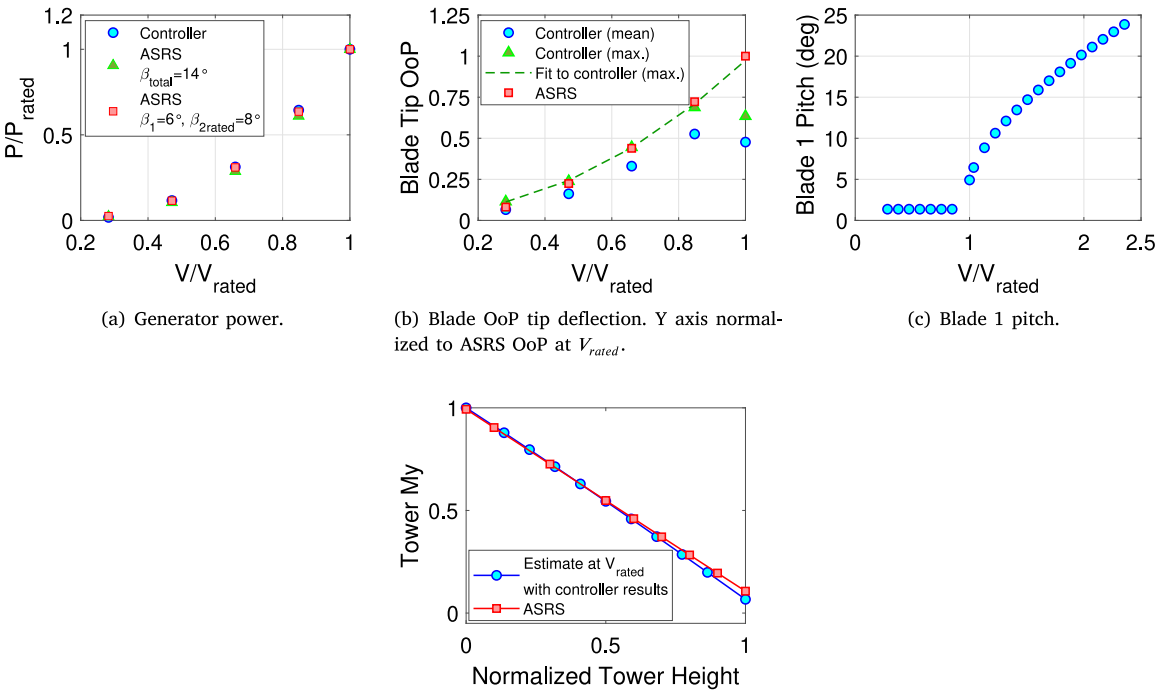

(a) Generator power.

(b) Blade OoP tip deflection. Y axis normalized to ASRS OoP at V_{rated}.

(c) Blade 1 pitch.

(d) Tower fore–aft moment (My). Y axis normalized to tower base moment estimate at V_{rated}.

Fig. 7. Comparison of ASRS to controller results for steady wind.

automated zeroth-order optimization method as described in Zalkind et al. [55]. In ASRS, the aerodynamic loads (Section 2.1) are obtained by emulating the baseline controller described above, which is achieved by maintaining constant blade pitch and TSR in Region 2, and by assuming that maximum thrust in steady wind occurs at rated wind speed (because the power in Region 3 would be regulated to the rated capacity of the turbine by pitching the blades).

The aero-servo-elastic simulations are performed using OpenFAST [56]. ElastoDyn is used to model the blades and tower. No waves are modeled because this work is focused on evaluating performance to wind loads. Fig. 7(a) shows the power curve of V2e up to the rated wind speed (V_{rated}). The controller results are obtained for steady wind and represent the average generator power over 400 s for each wind speed. Initially, in ASRS Level 1, the rated wind speed is estimated by assuming a constant $\beta_{total} = 14°$ and it matches well with the rated wind speed when using the controller. But β_{total} is not constant because the blade deflection (β_2) increases with higher wind speed. The change in blade deflection with wind speed, shown by the "$\beta_1 = 6°, \beta_{2_{rated}} = 8°$" curve, is calculated in ASRS Level 4 to obtain more accurate estimates of the power curve and AEP. This curve is in good agreement with the controller results; hence, the difference in AEP between ASRS and controller results is negligible as tabulated in Table 4.

Fig. 7(b) shows that the blade OoP tip deflection is generally in good agreement with the controller results (mostly with the "controller max". results for which the blade is in the upward position). A difference in deflection at the rated wind speed exists because the controller begins pitching the blades earlier, as shown in Fig. 7(c), to improve the load regulation at the transition between Regions 2 and 3. The dashed green curve in Fig. 7(b) is the result of fitting the "controller max". data points below the rated wind speed and plotting the results of the fit equation over the range of Region 2 wind speeds. This curve shows that if pitch remained constant, then the difference between the controller and ASRS deflection results would be small (2.67%) as shown in Table 4.

The tower fore–aft bending moments of ASRS are general in good agreement with the controller results as shown in Fig. 7(d) and Table 4. The ASRS tower base My (includes the effects of drag, overturning moment, weight of the rotor-nacelle-assembly or RNA, and tower self-weight) is less than 1% away from the controller results. DLCs 1.2 (power production in normal turbulence), 1.4 (power production in extreme coherent gust with wind direction change), 1.5 (power production in extreme wind shear), and 6.1 (parked turbine extreme wind speed model with 50-year recurrence period) were examined with the baseline controller to determine the extreme loads for the blade and tower. The ASRS extreme blade flapwise bending moments are calculated using rated aerodynamic loads calculated in ASRS Level 1 and scaled using the surrogate model discussed previously.

Fig. 8 shows that the ASRS blade flapwise bending moments agree with the controller extreme loads (that correspond to DLC 6.1) mostly outboard of 40% blade span; however, the ASRS root bending moment is more conservative than the controller results (12% greater) as tabulated in Table 4. The ASRS and DLC 6.1 controller blade out-of-plane tip deflection results are approximate as shown in Table 4. The surrogate model for extreme blade loads used in ASRS was created by first estimating the "total" bending moment distribution at rated and steady wind conditions (centrifugal and gravitational loads added to the aerodynamic loads estimated with blade element momentum theory), then running a sweep of operational and storm design load cases, and finally reconstructing the critical moment distribution at extreme load conditions by applying multiplicative factors from a polynomial tuning to the total bending moment distribution at rated and steady wind conditions [12]. However, in ASRS the extreme loads used in the blade structural optimization are a result of applying the polynomial tuning to the "aerodynamic" bending moments obtained at rated and steady wind. This may contribute to 6% larger blade tip deflection for the DLC 6.1 controller results and ASRS bending moments being more conservative in the inboard portion of the blade. However, the results presented herein show that reasonable and conservative estimates of extreme blade loads and blade deflection (which impacts tower clearance that is most important for upwind designs) can be obtained with ASRS.

Finally, the comparison of tower loads in Fig. 8(b) includes the ASRS results for steady wind at V_{rated} because the surrogate model only

Table 4
Comparison of ASRS to controller results for steady and extreme wind conditions.

Source	Steady wind			Extreme condition	
	Blade tip OoP (at V_{rated}) [m]	Tower base My (at V_{rated}) [MN m]	AEP [GWh/yr]	Blade root My [MN m]	Blade tip OoP [m]
ASRS	22.9	1039	133.6	329	31
Controller	22.3	1046	133.3	293 (DLC 6.1)	33 (DLC 6.1)
% difference	2.67%	−0.69%	0.21%	12.1%	−6.48%

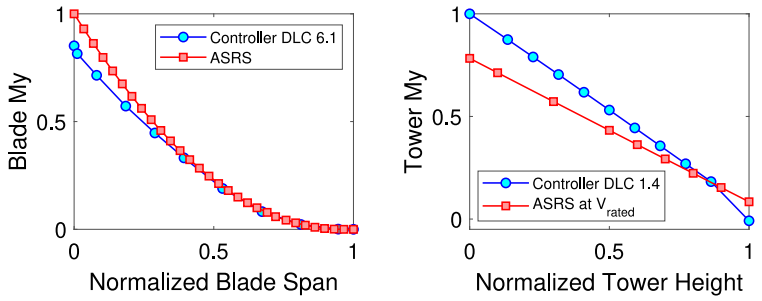

(a) Blade flapwise moment (My). Y axis normalized to ASRS blade root moment.

(b) Tower fore–aft moment (My). Y axis normalized to controller tower base moment.

Fig. 8. Comparison of ASRS blade and tower results to controller results. Blade results correspond to extreme condition. Tower ASRS results are for steady wind at V_{rated}.

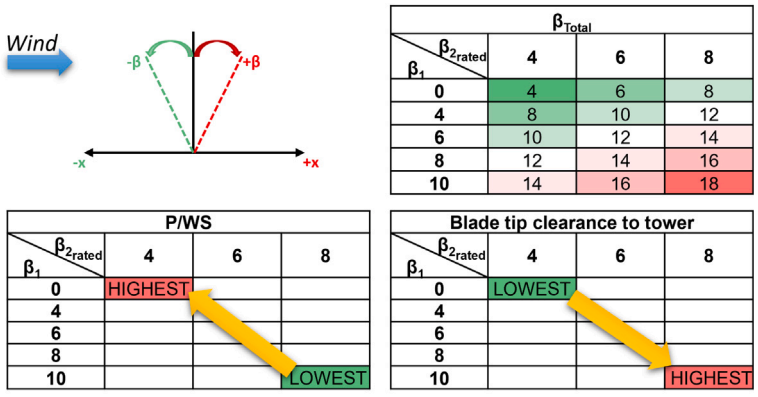

Fig. 9. Blade pre-cone and deflection angles studied for the V2e aerodynamic rotor design in downwind configuration.

applies to the blade loads. The controller extreme tower loads (which occur in DLC 1.4) are 20%–30% greater than the ASRS steady wind loads at rated wind speed for most of the tower span. This information is useful and applied to the tower aero-structural optimization for results shown in the next section. The blade flapwise and tower fore–aft directions (dominated by aerodynamic loads) drive the designs in deflection, strength, and buckling (particularly for the blade spar caps); hence, the loads in these directions are evaluated and compared to controller results. Gravitational and inertial loads are generally dominant in the blade edgewise and tower side-to-side directions (instead of the aerodynamic loads) and are important to analyze fatigue (which is not analyzed in this work). The ASRS blade edgewise loads only include aerodynamic effects and tower side-to-side loads do not include dynamic effects; thus, the blade edgewise and tower side-to-side loads are not compared to the controller results which include aerodynamic, gravitational, and inertial effects.

5. Results

In this section, results for three different case studies where ASRS is applied are presented: (1) variation of blade pre-cone and load alignment via blade deflection, (2) evaluation of 25 different pre-defined aerodynamic designs that vary in number of blades, blade length, axial induction factor, and airfoil family, and (3) comparison of downwind versus upwind rotor configurations.

5.1. Case study 1: Blade pre-cone vs. Passive load alignment via blade deflection

The ASRS approach is applied to study the effect of different blade pre-cone angles (β_1) and different blade deflection levels (β_2) for passive load alleviation. The aerodynamic V2e downwind design is selected for this study and evaluated for $\beta_1(°) = [0, 4, 6, 8, 10]$ and $\beta_{2_{rated}}(°) = [4, 6, 8]$ (equivalent to tip deflection of 7%–14% of the blade length at V_{rated}). Deflections and angles that are downwind are positive as shown in Fig. 9. The top right table of Fig. 9 shows fifteen combinations and eight unique β_{total} angles (which are input to the AD15 input file to calculate aerodynamic loads). The bottom two tables of Fig. 9 show the assumption that larger β_{total} results in lower power per wind speed because the rotor swept area is reduced, but larger β_{total} also increases the blade tip-to-tower clearance.

In this work, 25 MW of power must be achieved; thus, the rated wind speed changes for the various combinations of pre-cone and passive cone angles because of the change in the rotor swept area. Larger β_{total} reduces the rotor swept area which leads to achieving 25 MW of power at a higher rated wind speed as shown by the right

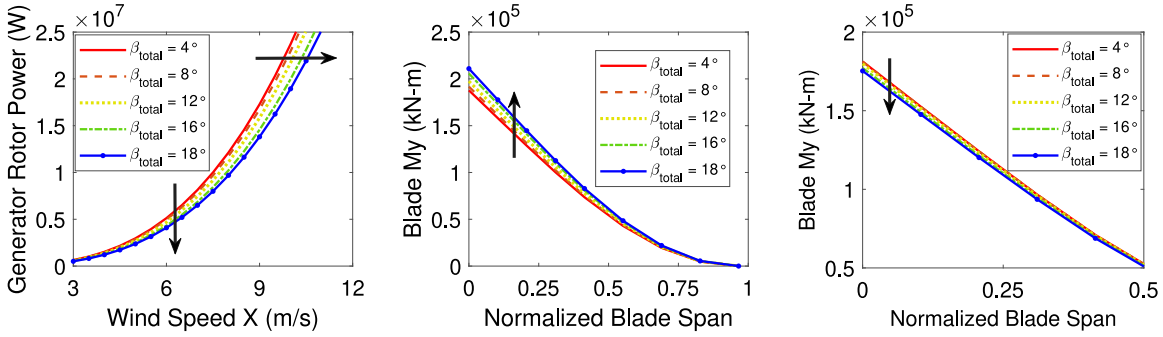

(a) Generator power (b) Flapwise bending moment at varying $V = V_{rated}$ (c) Flapwise bending moment at fixed V = 10 m/s

Fig. 10. Change in aerodynamic performance due to the change in β_{total}.

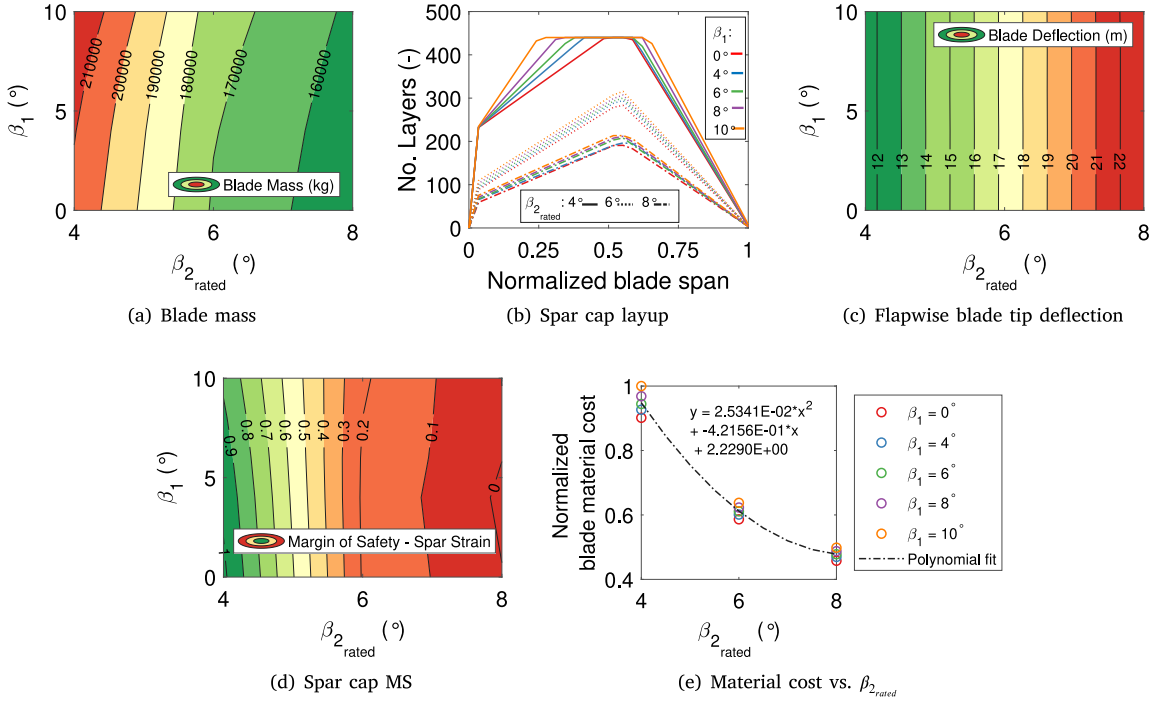

(a) Blade mass (b) Spar cap layup (c) Flapwise blade tip deflection

(d) Spar cap MS (e) Material cost vs. $\beta_{2_{rated}}$

Fig. 11. ASRS Level 2 blade structural optimization results for V2e design.

horizontal arrow in Fig. 10(a). Higher rated wind speeds (resultant of larger β_{total}) increase the blade flapwise bending moments as shown in Fig. 10(b). Larger β_{total} reduces the power per wind speed as shown by the downward vertical arrow in Fig. 10(a). If achieving 25 MW was not a requirement and the aerodynamic design was not modified, then the turbine is derated and blade bending moments at a fixed wind speed reduce due to larger β_{total} as exemplified in Fig. 10(c) for a wind speed of 10 m/s.

The structural optimization results of the blade are shown in Fig. 11. The blade mass and cost reduce for larger $\beta_{2_{rated}}$ due to the reduction of spar cap material (carbon) quantity required to meet the optimization constraints of deflection (at rated wind speed) and strain (with extreme loads). Heavier designs are obtained for larger β_1 (and consequently β_{total}) because rated power is achieved at higher wind speeds that increase blade loads. Fig. 11(e) shows that the relationship between the blade material cost and $\beta_{2_{rated}}$ can be described with a quadratic function. The deflection constraints are always active, but the spar margin of safety becomes more active for designs with larger blade deflection as is illustrated in Fig. 11(d).

The results obtained from ASRS Levels 1 and 2 are inputs to the aero-structural optimization of the support structure for which results are shown in Fig. 12. The resultant designs meet all the defined constraints, the optimization is driven by the bending stress in the fore–aft direction at the base, and the upper limit of the base outer diameter is active (15 m at the base and 6.82 m at the top).

The optimizer minimizes the support structure mass by using the maximum base diameter and adjusting the wall thickness to meet the strength constraint. The mass of the support structure depends more significantly on the pre-cone angle of the blades because this has a higher effect on the RNA overturning moment as illustrated by Fig. 13. The difference in thrust for different $\beta_{2_{rated}}$ angles for the same pre-cone is small and the bending moment at the base due to drag increases for larger pre-cone and blade deflection angles because of the change in rated wind speed corresponding to the β_{total} angle. Overall, blade deflection is not a concern for this downwind design as the blades deflect away from the tower. Spring back motions due to the blades passing through the tower wake should be considered in higher fidelity design and analysis. The tower top stresses are well below the stress limit (233 MPa) and the optimizer drives the base

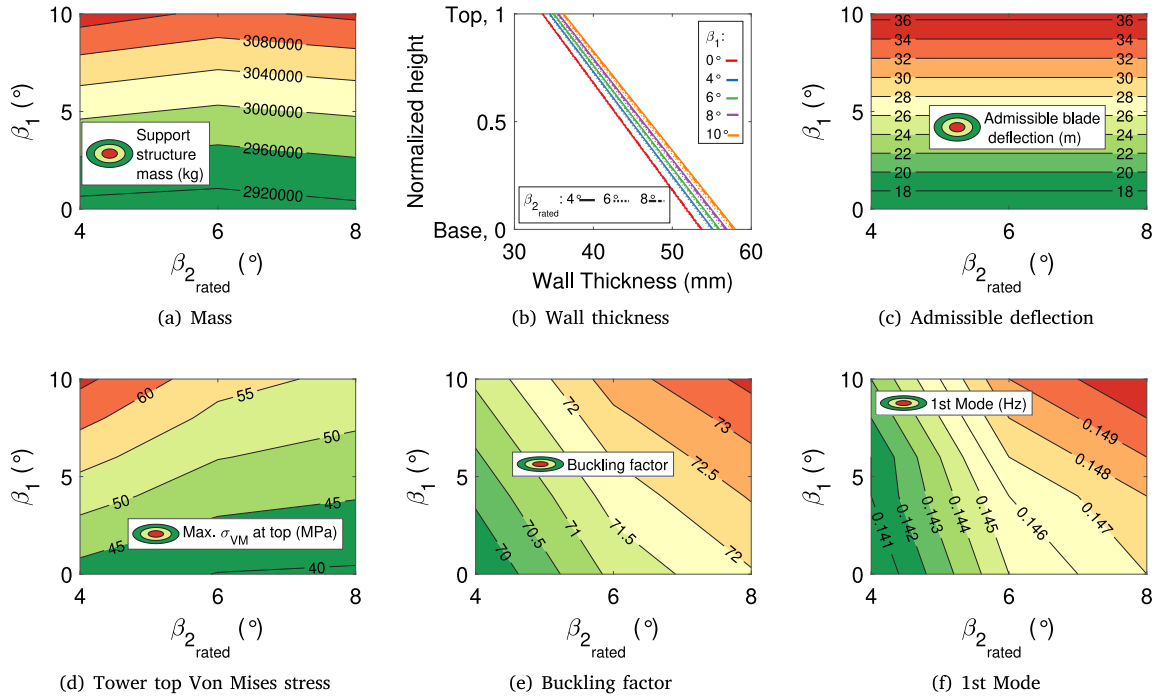

(a) Mass (b) Wall thickness (c) Admissible deflection

(d) Tower top Von Mises stress (e) Buckling factor (f) 1st Mode

Fig. 12. ASRS Level 3 support structure aero-structural optimization results for V2e design.

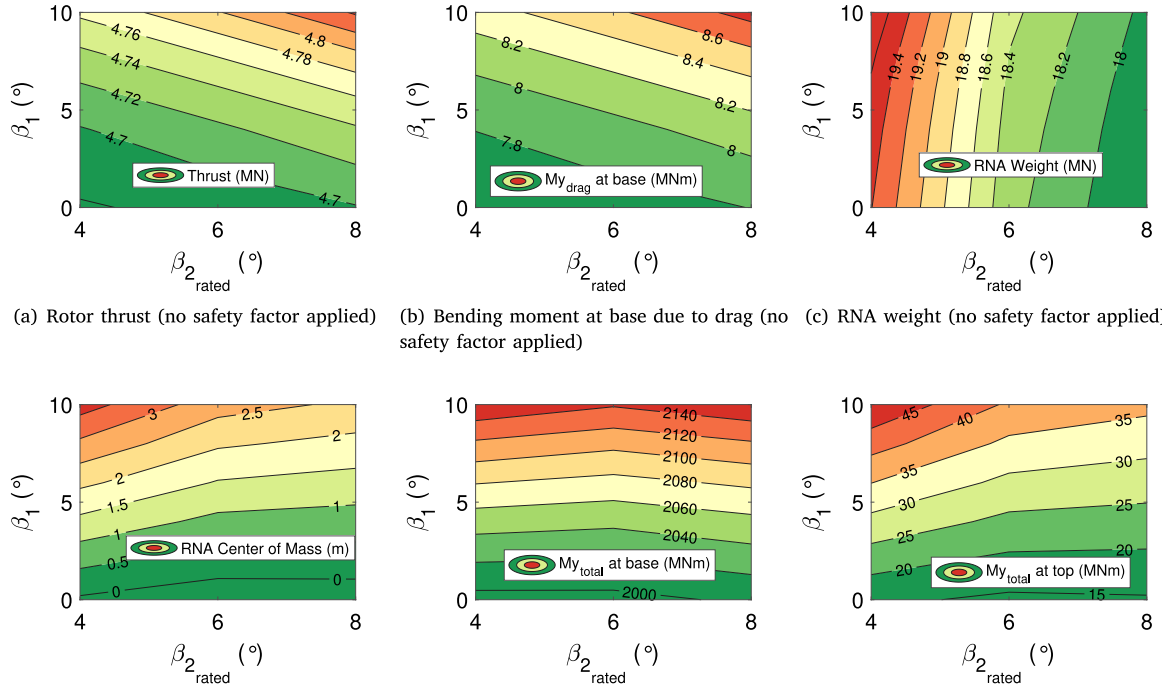

(a) Rotor thrust (no safety factor applied) (b) Bending moment at base due to drag (no safety factor applied) (c) RNA weight (no safety factor applied)

(d) RNA center of mass along wind direction (e) Fore–aft bending moment at base (f) Fore–aft bending moment at top

Fig. 13. Loads applied in ASRS Level 3 support structure aero–structural optimization of V2e.

of the support structure to have a maximum stress equal to the stress limit to minimize mass. The tower top stresses are mainly due to the RNA overturning moment which increases for large pre-cone angles and heavy/stiff blades (small $\beta_{2_{rated}}$). Buckling does not dominate the results and may be underestimated due to the formulation only taking into account axial loads and not the effect of bending loads, but this can be further investigated in higher fidelity analyses.

Fig. 14 provides a summary of the turbine designs (rotor, tower, and monopile) obtained with ASRS including power curves, mass, AEP, and LCOE. Fig. 14(a) shows the final power curves that maintain the assumed $\beta_{2_{rated}}$ at rated wind speed as shown in Fig. 14(b), and use the profile of passive load alleviation achieved through blade deflection to estimate AEP through an iterative process. Larger pre-cone and blade deflection angles reduce the power per wind speed as expected and rated power is achieved at higher wind speeds, which

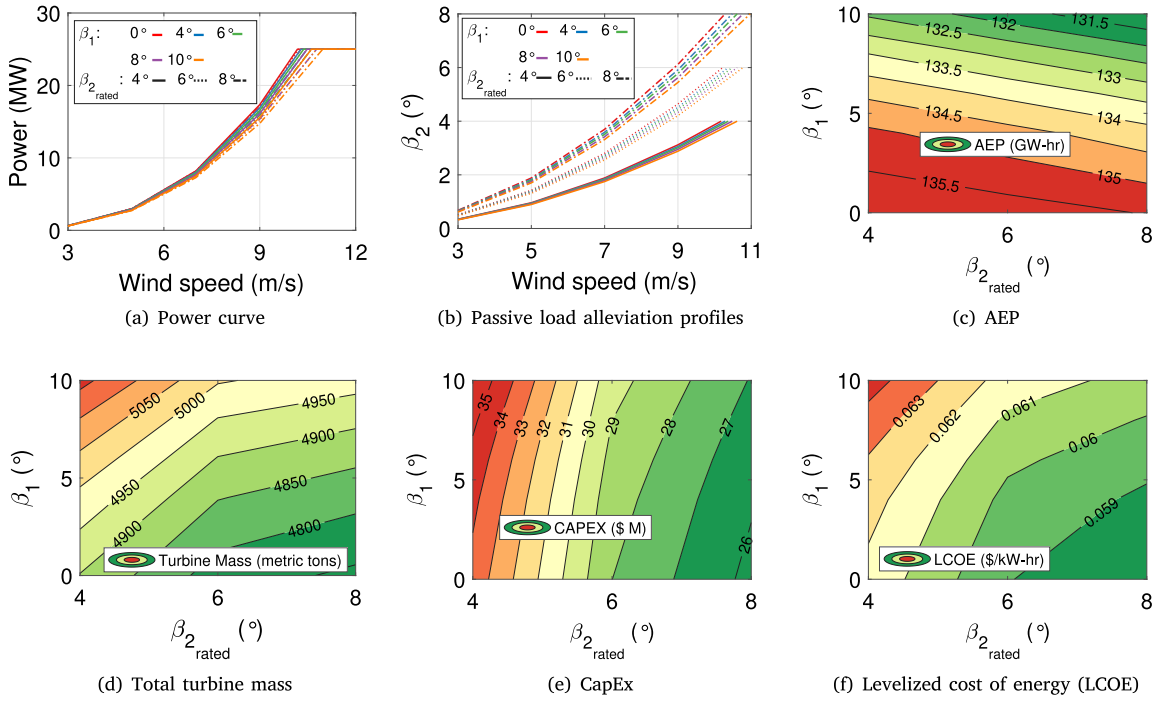

(a) Power curve (b) Passive load alleviation profiles (c) AEP

(d) Total turbine mass (e) CapEx (f) Levelized cost of energy (LCOE)

Fig. 14. ASRS Level 4 LCOE calculation results for various blade pre-cone and flapwise deflection values at rated wind speed.

affect the AEP shown in Fig. 14(c) where the largest AEP corresponds to the lowest β_{total}. The total turbine mass is largest for large pre-cone angles and low blade deflection angles because stiff blades are heavy and increase the overturning moment that consequently increases the support structure mass, and also higher β_{total} angles increase the rotor thrust and tower drag due to rated power being achieved at higher wind speeds. Fig. 14(e) shows that variations in CapEx are mainly due to the different levels of passive load alleviation ($\beta_{2_{rated}}$). Consequently, the LCOE shown in Fig. 14(f) can be reduced by up to 7.8% by selecting a design with low pre-cone and on the higher end of the studied passive load alleviation (flapwise deflection).

5.2. Case study 2: Rapid screening of 25 downwind aerodynamic designs

The 25 different aerodynamic designs presented in Fig. 6 are studied here for a fixed pre-cone angle $\beta_1 = 6°$ and passive load alleviation equivalent to $\beta_{2_{rated}} = 8°$ with a comparison of the design results and performance. Structurally, all the designs have the two webs that extend from approximately 13% to 95% blade span (with minor adjustments for each blade aerodynamic design based upon its blade span stations and tip taper), the number of tri-axial fiberglass layers at the root was determined based on the root bending moment and using a simple bending moment equation, the width of the spar caps (or distance between webs) is defined in terms of percent of chord, and all designs taper the spar cap width near the tip similarly. By fixing the objective value of $\beta_{2_{rated}}$ to 8°, it is possible to capture the geometric effect of the different blade sizes (length and chord) on the optimization of the spar cap layup and it facilitates comparative analyses.

The results of the 25 aerodynamic designs are classified based on result type and evaluated with a correlation analysis to determine trends. The correlation analysis served as initial guidance because it only helps identify linear relationships among two result types. Thus, further inspection was performed to check the linear trends identified with correlation analysis and analyze other results that do not indicate strong linear dependence. Correlation coefficients and the null hypothesis test values are obtained with the "corrcoef" function of MATLAB. The correlation coefficients indicate whether there exists linear dependence between result types (values range from −1 or negative correlation to 1 or positive correlation) and the null hypothesis values indicate the significance level of the correlation (off-diagonal values close to zero indicate strong significance).

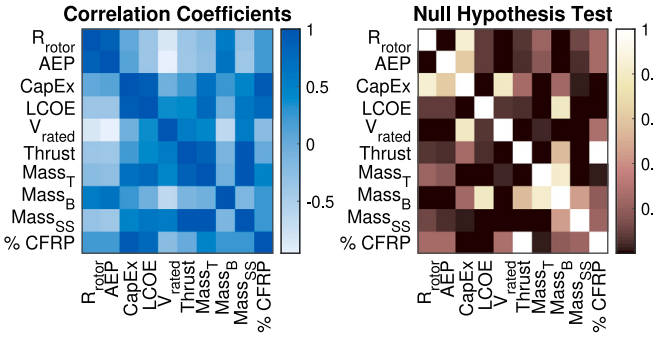

Fig. 15. Correlation analysis results using the outputs of the 25 aerodynamic designs as observations.

Fig. 15 shows the correlation analysis results. Some of the result types with significant linear dependence are the rotor radius (R_{rotor}) to AEP, rated wind speed (V_{rated}), and blade mass ($Mass_B$), LCOE to the turbine CapEx, percent of carbon fiber reinforced plastic (CFRP) on the blade mass, rated Thrust to rated V_{rated}, and the mass of the turbine ($Mass_T$) and the support structure ($Mass_{SS}$) to the rated Thrust. These linear relationships identified with the correlation analysis in addition to other relationships among other combination of result types that may not show strong linear dependence (but that could have non-linear dependence) are studied further.

Fig. 16 shows that the mass of the turbine increases with rotor radius, but designs with axial induction of $a = 1/4$ have lower mass than those with $a = 1/3$ because low axial induction factor designs have lower thrust as shown in Fig. 17 which significantly reduces the mass of the support structure as shown in Fig. 18. The turbine mass of designs with two-bladed (2-b) rotors is generally smaller than with three-bladed (3-b) rotors because they have one less blade.

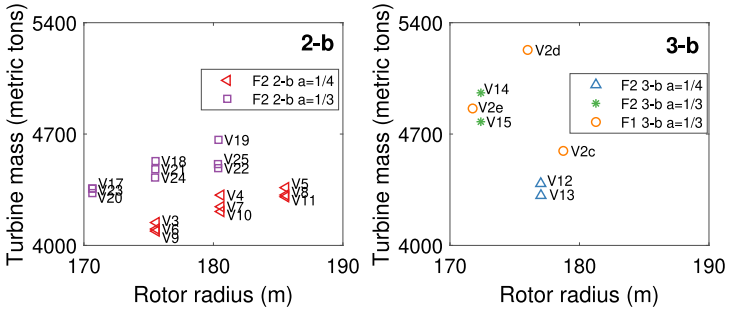

Fig. 16. Turbine mass (blades, hub, nacelle, and support structure) versus rotor radius for two-bladed (2–b) and three–bladed designs (3–b).

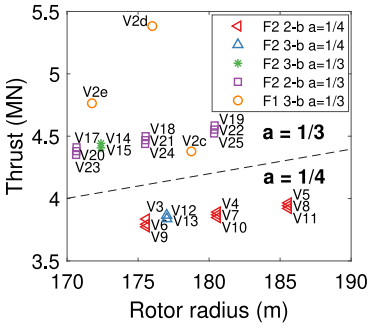

Fig. 17. Rated thrust versus rotor radius.

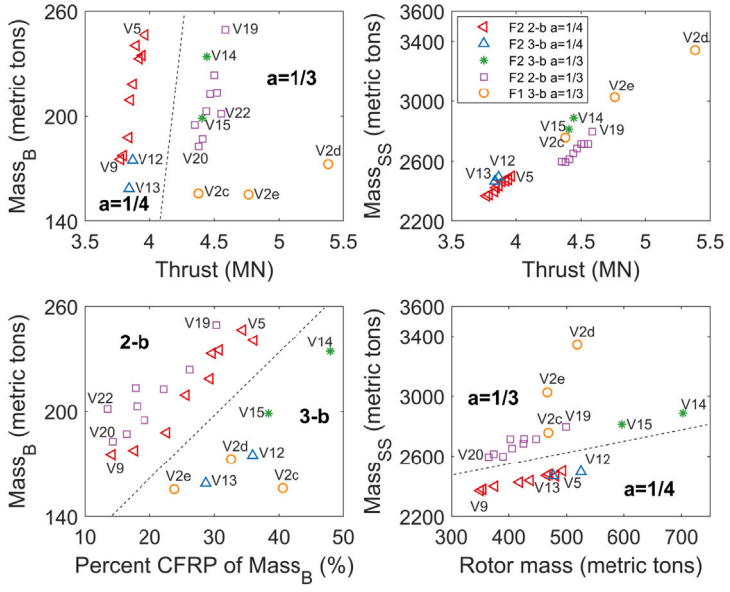

Fig. 18. Mass of blade and support structure versus rated thrust.

Fig. 18 shows blade mass is not highly dependent on the rotor thrust and that similar results may be obtained with a = 1/4 and a = 1/3. Since the spar cap is the structural component optimized, then the blade mass is significantly dependent on the percent of CFRP on the blade mass which depends on the blade loads and the geometry of the blade (chord, twist, and thickness) with the F1-airfoil designs (larger thickness that increases area moment of inertia and reduces the need for thick spar caps) resulting in lower mass than the F2 designs (lower airfoil thickness). The effect of the rotor mass (mass of blades that changes the support structure loads due to the RNA) on the mass of the support structure is also shown and it is significant but not as steep compared to the relationship with thrust.

The CapEx results shown in Fig. 19 are significantly dependent on the blade mass mainly because of the expensive carbon used in the spar caps. CapEx is higher for three-bladed designs than two-bladed because of the extra blade. Fig. 20 shows that AEP reduces when rated power is achieved at higher wind speeds. The low-axial factor designs (a = 1/4) have in general lower rated wind speed than the designs with a = 1/3. Rated power can be achieved at lower wind speeds by increasing the rotor radius. Also, the results show that two-bladed and three-bladed rotors can be designed to have similar rated wind speed and AEP.

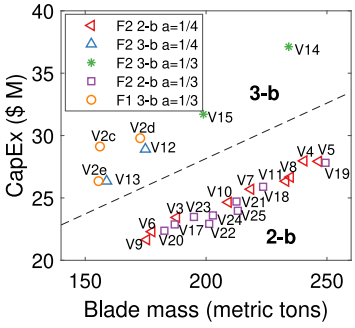

Fig. 19. CapEx versus blade mass.

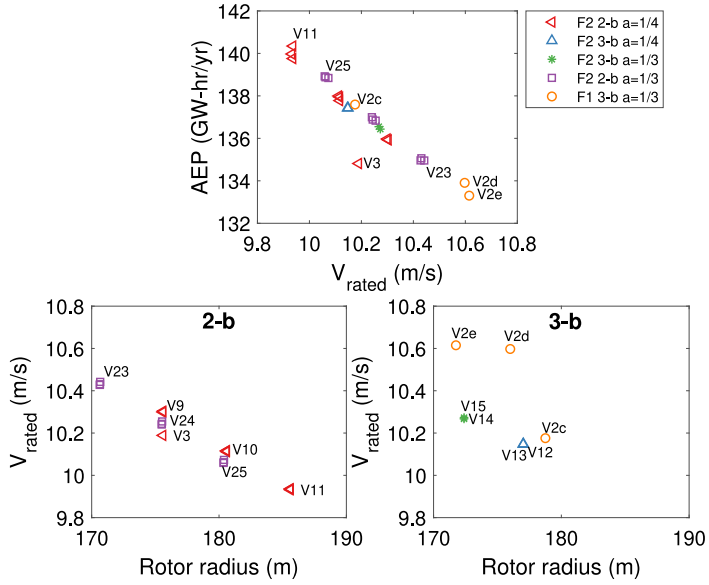

Fig. 20. AEP and rated wind speed in relation to rotor radius.

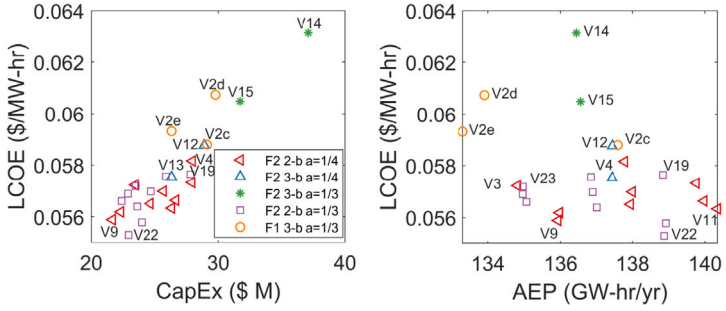

Fig. 21. LCOE in relation to CapEx and AEP.

Finally, we examine the effect of CapEx and AEP on LCOE in Fig. 21. LCOE has significant linear dependence to CapEx that is a result of the dependence of CapEx to the blade mass (expensive carbon in spar caps) and the thrust that dominates the changes in the support structure mass. Despite that a linear relationship between AEP and LCOE is not observed, in general designs with higher AEP have lower LCOE as expected. It is observed that in general three-bladed designs have higher LCOE than two-bladed designs. The design V14 has the highest LCOE that is approximately 12.4% higher compared to V22.

A summary of the designs with best performance (lowest LCOE, CapEx, and Turbine Mass, and highest AEP) are shown in Table 5 for $\beta_1 = 6°$ and $\beta_{2_{rated}} = 8°$. This shows that different designs are preferred depending on the chosen metric. It is also important to note that the LCOE obtained does not account for changes in operational expenditures (OpEx) which are significant for offshore turbines, and thus evaluating the designs with various metrics is important. Despite that in general two-bladed designs outperform three-bladed designs, further analysis that includes high-fidelity control design and higher-fidelity cost analysis would be required to fully assess the trade-offs between two and three bladed rotors. However, the analyses shown herein with ASRS are helpful to rapidly evaluate designs and determine trade-offs that can help downselect from the large design space, and

Table 5
Summary of designs with best performance for $\beta_1 = 6°$ and $\beta_{2_{rated}} = 8°$.

Characteristics				LCOE		AEP		CapEx		Turbine mass	
Group	Airfoil family	No. blades	a	($/MW-h)	Design	(GW-h/yr)	Design	($ M)	Design	(metric tons)	Design
1	F2	2	0.250	0.056	V9	140.3	V11	21.7	V9	4090	V9
2	F2	3	0.250	0.058	V13	137.4	V12	26.3	V13	4314	V13
3	F2	3	0.333	0.060	V15	136.6	V15	31.7	V15	4778	V15
4	F2	2	0.333	0.055	V22	138.9	V25	22.4	V20	4329	V20
5	F1	3	0.333	0.059	V2c	137.6	V2c	26.3	V2e	4594	V2c
Overall two-bladed				0.055	V22	140.3	V11	21.7	V9	4090	V9
Overall three-bladed				0.058	V13	137.6	V2c	26.3	V13	4314	V13

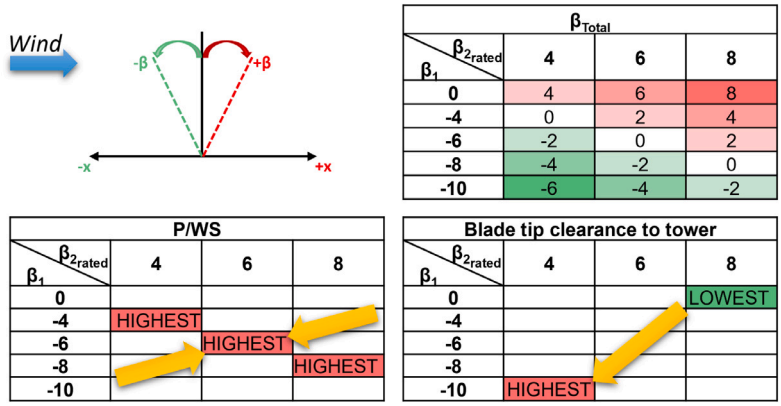

Fig. 22. Blade pre-cone and passive load alleviation angles used to study the V2e aerodynamic rotor design in upwind configuration.

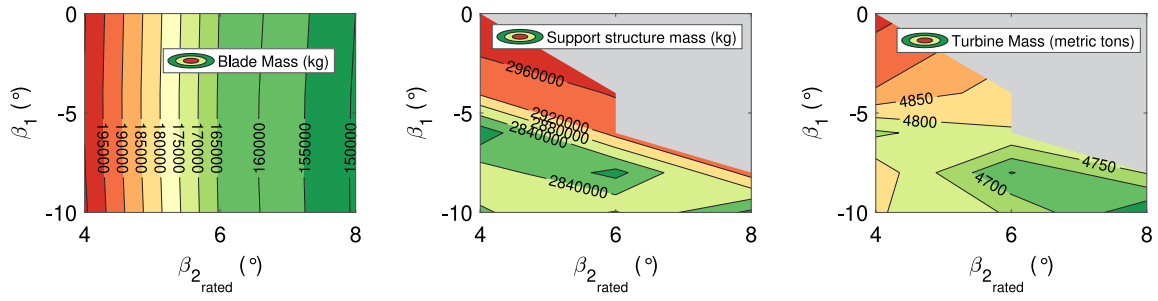

(a) Blade mass (b) Support structure mass (c) Total turbine mass

Fig. 23. ASRS mass results for V2e in upwind configuration.

downselected designs can be chosen for further study. Even though in this case study, the aerodynamic designs were studied for a single combination of β_1 and $\beta_{2_{rated}}$, more combinations could be studied for each design using the ASRS approach.

5.3. Case study 3: Upwind vs. Downwind analysis for 25 MW V2e design

The aerodynamic V2e design is studied assuming an upwind configuration and the results are compared to the downwind results of Case Study 1. The study is performed assuming the same $\beta_{2_{rated}}$ as in Case Study 1 (4, 6, and 8 degrees), and the pre-cone angles are adjusted for upwind configurations ($\beta_1(°) = [0, -4, -6, -8, -10]$). In total, fifteen cases are studied (out of which nine have unique β_{total} angles) as shown in Fig. 22. Larger β_{total} values are expected to reduce the power per wind speed. However, in an upwind configuration the blade deflection is towards the tower and reduces the value of β_{total} compared to a downwind configuration; thus, tower clearance is more important for upwind turbines.

Fig. 23 shows resultant mass for the blade, support structure, and total turbine (blades, hub, nacelle, and support structure). The blade mass is less dependent on β_1 compared to the downwind results because the upwind β_{total} values are lower and result in less differences in the blade loads for all cases analyzed. A feasible solution for the aero-structural optimization of the support structure was not found for four cases (which have low pre-bend and high blade deflection) because the blade deflection (due to extreme loads) exceeded the admissible blade deflection. The unfeasible areas are indicated with gray background.

Fig. 24 shows the passive load alleviation profile, resultant power curve, and the LCOE components for the V2e turbine in upwind configuration. In this case, the highest AEP in Fig. 24(a) is not obtained for the lowest pre-bend and blade deflection, but for the combination that resulted in the lowest β_{total}, as expected. Fig. 24(b) shows that multiple ways of achieving the same deflection at rated wind speed exist, and that the deflection versus wind speed (passive load alleviation profile) can be tailored to maximize different functions. Fig. 24(d) shows the admissible blade deflection with a colored contour plot and the blade deflection due to extreme loads (from surrogate model) is overlaid on top. The unfeasible solutions are to the right of the white dashed line because the blade deflection exceeds the admissible blade deflection. The percentage changes in blade cost are more significant than the changes in the support structure for the various combinations of β_1 and $\beta_{2_{rated}}$; thus, CapEx and LCOE results have a trend similar to the

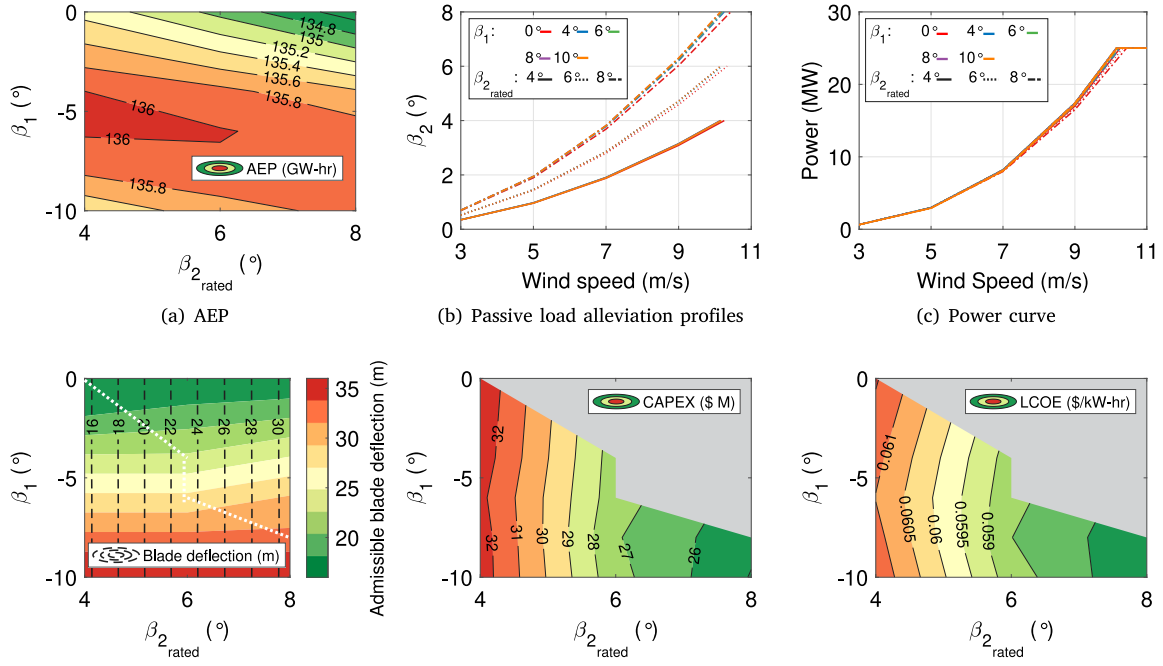

(a) AEP (b) Passive load alleviation profiles (c) Power curve

(d) Admissible blade deflection vs. extreme blade deflection (e) CapEx (f) Levelized cost of energy (LCOE)

Fig. 24. ASRS results for V2e in upwind configuration.

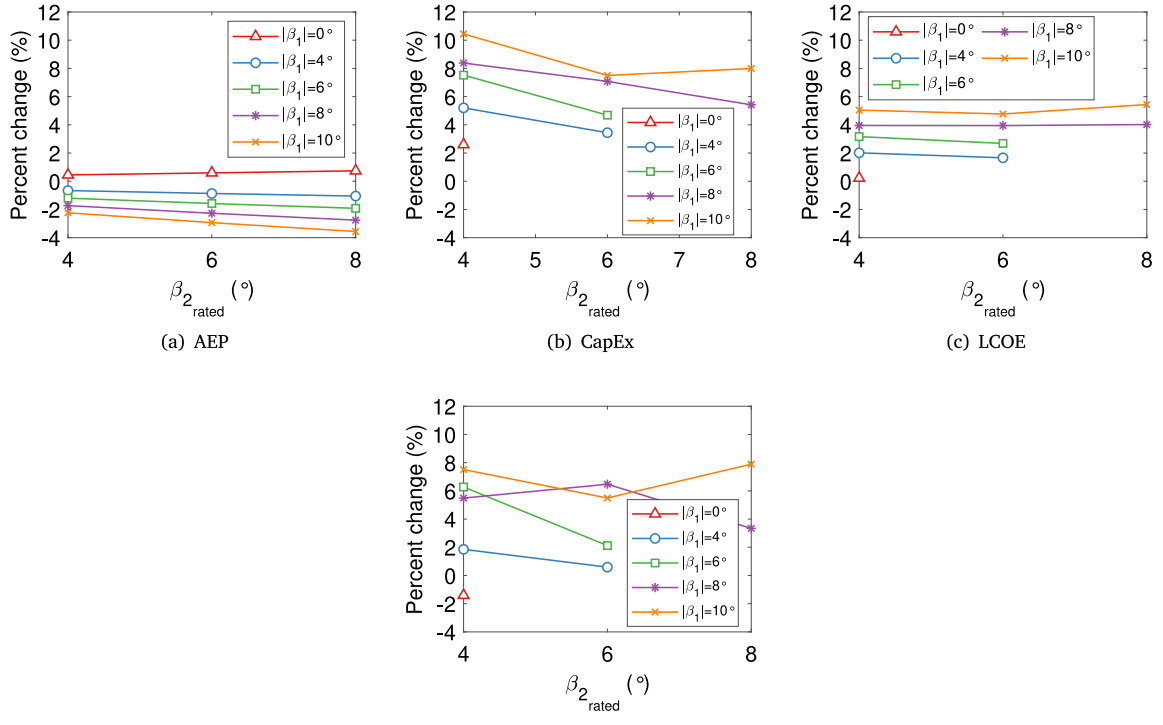

(a) AEP (b) CapEx (c) LCOE

(d) Turbine mass

Fig. 25. Comparison of V2e downwind to upwind results.

blade mass and the lowest LCOE corresponds to the combinations with highest blade deflection.

Fig. 25 shows the percent change of downwind results relative to the upwind results for each combination of β_1 and $\beta_{2_{rated}}$ values studied. For most combinations, downwind results have lower AEP or higher mass/CapEx/LCOE except for options with the lowest pre-cone angle. However, as shown in Tables 6–7, the best downwind options (highest AEP and lowest mass/CapEx/LCOE) occur at different combinations of β_1 and $\beta_{2_{rated}}$ values compared to upwind. Both upwind and downwind show that higher deflection is preferred to reduce mass, CapEx, and LCOE given that the blades include expensive carbon and the percent change in the support structure cost was relatively small. The best

Table 6
Comparison of maximum, minimum, and best downwind to upwind results.

Result type	Units	Maximum		Minimum		Best		
		Down	Up	Down	Up	Down	Up	Diff.
AEP	GW-h	135.9	136.0	131.0	134.5	135.9	136.0	−0.1%
Mass	metric tons	5166	4967	4739	4607	4739	4607	2.9%
CapEx	$ M	35.90	32.79	25.74	24.94	25.74	24.94	3.2%
LCOE	$/MW-h	0.0645	0.0616	0.0581	0.0575	0.0581	0.0575	1.0%

Table 7
Corresponding β_1 and $\beta_{2_{rated}}$ values of maximum, minimum, and best downwind to upwind results.

Result type	Angle (°)	Maximum		Minimum		Best	
		Down	Up	Down	Up	Down	Up
AEP	β_1	0	−6	10	0	0	−6
	$\beta_{2_{rated}}$	4	4	8	8	4	4
	β_{total}	4 (minimum)	−2	18 (maximum)	8	4 (minimum)	−2
Mass, CapEx, and LCOE	β_1	10	0	0	−10	0	−10
	$\beta_{2_{rated}}$	4	4	8	8	8	8
	β_{total}	14	4	8	−2	8	−2

options for the downwind and upwind configurations have similar values, but the upwind configuration slightly outperforms the downwind configuration. Further analysis that include design and simulations with a high fidelity controller can be performed on downselected options and settings identified with ASRS to study trade-offs of downwind and upwind designs, which requires much less time.

6. Conclusions and future work

The development of large-scale wind turbines is challenged by the growth in loads, mass, and cost, and by the blade flexibility that impacts power capture and tower clearance. Additional limiting factors for the development of new timely and robust designs, of the blades and tower and monopile support structures, are the long duration design iterations and challenges of integrating innovations (two-bladed, downwind, low-axial induction, and passive load alleviation) using standard sequential design processes. In this work, we developed and demonstrated the ASRS design approach to overcome these limitations and answer open research questions for large-scale turbine design. ASRS is a multilevel multidisciplinary optimization approach that emulates a baseline turbine controller and includes evaluation of aerodynamic rotor loads, blade structural optimization using detailed composite layups, aero-structural optimization of the support structure (tower and monopile), and LCOE estimation. ASRS utilizes the blade deflection/passive cone as a new design variable for passive load alleviation via load alignment to obtain better load estimates, tailor the power curve to maximize AEP, and minimize turbine mass. The design approach is illustrated with an investigation of offshore fixed-bottom 25 MW wind turbines to determine trends and trade-offs that reduce mass, CapEx, and LCOE and increase AEP among others. Three case studies are performed to demonstrate the accuracy, efficiency, and versatility of ASRS: (1) blade pre-cone versus passive load alleviation via blade deflection, (2) rapid screening of 25 different rotor aerodynamic designs (which vary in number of blades, axial induction factor, blade length, and airfoil family) for fixed pre-cone and passive cone angles, and (3) downwind versus upwind study.

Case studies 1 and 3 show that the designer can reduce turbine mass, LCOE, and CapEx by choosing high blade deflection and selecting a pre-cone angle that maximizes AEP and meets tower clearance requirements. In downwind and upwind configurations, high blade deflection is preferred to reduce LCOE, CapEx, and mass, but the selection of pre-cone depends on the turbine orientation relative to the incoming wind. Allowing the blades deflect to more has significant advantage for larger offshore turbines as discussed above, but may create challenges on the control system design and in the fatigue performance, which can be evaluated in further and higher-fidelity analysis.

The two-bladed designs studied herein show significant advantages in LCOE, AEP, turbine mass, and CapEx compared to three-bladed designs. Operational expenditures may also reduce for two-bladed designs because they have one less blade that has to be transported, installed, and maintained. It is shown that the two-bladed designs studied can be less, equal, or better performing than three-bladed options depending on their aerodynamic design. But further study is required to evaluate additional aspects of two and three-bladed rotors such as the inherent yaw-dependence mass moment of inertia and its effect on the turbine control design.

Low-axial induction factor (a = 1/4) designs shown herein have lower chord and lower thrust, but longer blade length to achieve the same rated power. The smart design of low-axial induction factor rotors results in designs with comparable or better AEP and LCOE than designs with typical a = 1/3. Low-axial induction factors enable lower turbine CapEx and mass because the blades have smaller chord and lower thrust (the latter significantly reduces the mass of the support structure). The performance of low-axial induction factor designs seems promising and further study would be beneficial to determine the fatigue and ultimate limit state performance using a full DLC analysis.

The study of downwind versus upwind with ASRS shows that the best upwind designs slightly outperform the best downwind designs in CapEx (3%), mass (3%), AEP (0.1%), and LCOE (1%). Also, the best configurations for upwind and downwind are not necessarily the same and similar performance may not be obtained by simply placing the rotor on the other side of the tower and mirroring the pre-cone angle. Instead, the total pre-cone angle (accounts for the pre-cone and blade deflection) should be matched. Downwind turbines can still be attractive as they allow relaxing the tower clearance constraint as wind turbines continue to grow larger. Further analysis with a high-fidelity controller and DLC analysis considering tower shadow will help answer open research questions.

In this work, we demonstrate the use of blade deflection to design the passive load alleviation profile via load alignment. This could be further studied by considering bend–twist coupling in the blade aerodynamic and structural design (the blade geometry and the layup including material type, quantity, and ply angles) to maximize AEP (reduce the power curve arc-length) and minimize blade cost. Such analysis may require higher fidelity aerodynamic and structural tools. Further research is needed to include fatigue as a constraint in the rapid optimization through surrogate modeling that requires significant validation with aero-servo-elastic simulations using turbulent wind. The shaft tilt angle may be studied as an additional design variable to

maximize the rotor swept area, AEP, and reduce gravitational bending moments on the tower.

CRediT authorship contribution statement

Alejandra S. Escalera Mendoza: Conceptualization, Methodology, Software, Formal analysis, Investigation, Data curation, Writing – original draft, Writing – review & editing, Visualization. **D. Todd Griffith:** Conceptualization, Methodology, Investigation, Data curation, Writing – original draft, Writing – review & editing, Supervision, Funding acquisition. **Michael Jeong:** Methodology, Software, Formal analysis, Writing – review & editing. **Chris Qin:** Methodology, Software, Writing – review & editing. **Eric Loth:** Conceptualization, Investigation, Writing – review & editing. **Mandar Phadnis:** Software, Formal analysis, Writing – original draft, Writing – review & editing. **Lucy Pao:** Conceptualization, Investigation, Writing – review & editing. **Michael S. Selig:** Conceptualization, Formal analysis, Investigation, Writing – review & editing.

Declaration of competing interest

The authors declare the following financial interests/personal relationships which may be considered as potential competing interests: The author(s) disclosed receipt of the following financial support for the research, authorship and/or publication of this article: This work was supported by the U.S. Department of Energy Advanced Research Projects Agency-Energy (ARPA-E) under the Segmented Ultralight Morphing Rotor project [award number DE-AR0000667].

Data availability

The data that support the findings of this study are not openly shared due to confidentiality. Limited data may be shared from D. Todd Griffith (tgriffith@utdallas.edu) upon reasonable request.

Acknowledgments

The authors are grateful for the support of the ARPA-E program and staff. The authors acknowledge the support of the entire SUMR team. Any opinions, findings, and conclusions or recommendations expressed in this material are those of the authors and do not necessarily reflect the views of ARPA-E.

Funding

The author(s) disclosed receipt of the following financial support for the research, authorship and/or publication of this article: This work was supported by the U.S. Department of Energy Advanced Research Projects Agency-Energy (ARPA-E) under the Segmented Ultralight Morphing Rotor project [award number DE-AR0000667].

References

[1] A.S. Escalera Mendoza, D.T. Griffith, C. Qin, E. Loth, N. Johnson, Rapid approach for structural design of the tower and monopile for a series of 25 MW offshore turbines, J. Phys. Conf. Ser. 2265 (3) (2022) 10, http://dx.doi.org/10.1088/1742-6596/2265/3/032030.

[2] C.C. Qin, E. Loth, N. Johnson, P. Bortolotti, A.S. Escalera Mendoza, D.T. Griffith, L.Y. Pao, K. Johnson, An explicit LCOE model for fixed-bottom offshore wind turbines, 2023, in preparation.

[3] S. Yao, M. Chetan, D.T. Griffith, Structural design and optimization of a series of 13.2 MW downwind rotors, Wind Eng. 45 (6) (2021) 1459–1478, http://dx.doi.org/10.1177/0309524X20984164.

[4] M. Chetan, S. Yao, D.T. Griffith, Multi-fidelity digital twin structural model for a sub-scale downwind wind turbine rotor blade, Wind Energy 24 (12) (2021) 1368–1387, http://dx.doi.org/10.1002/we.2636.

[5] C.C. Qin, E. Loth, D.S. Zalkind, L.Y. Pao, S. Yao, D.T. Griffith, M.S. Selig, R. Damiani, Downwind coning concept rotor for a 25 MW offshore wind turbine, Renew. Energy 156 (2020) 314–327, http://dx.doi.org/10.1016/j.renene.2020.04.039.

[6] A.S. Escalera Mendoza, S. Yao, M. Chetan, D.T. Griffith, Design and analysis of a segmented blade for a 50 MW wind turbine rotor, Wind Eng. 46 (4) (2022) 1146–1172, http://dx.doi.org/10.1177/0309524X211069393.

[7] S. Kianbakht, D. Martin, K. Johnson, D. Zalkind, L. Pao, E. Loth, J. Simpson, S. Yao, M. Chetan, D.T. Griffith, Design space exploration and decision-making for a segmented ultralight morphing 50-MW wind turbine, Wind Energy 25 (12) (2022) 2016–2035, http://dx.doi.org/10.1002/we.2781.

[8] K. Maki, R. Sbragio, N. Vlahopoulos, System design of a wind turbine using a multi-level optimization approach, Renew. Energy 43 (2012) 101–110, http://dx.doi.org/10.1016/j.renene.2011.11.027.

[9] C.L. Bottasso, F. Campagnolo, A. Croce, S. Dilli, F. Gualdoni, M.B. Nielsen, Structural optimization of wind turbine rotor blades by multilevel sectional/multibody/3D-FEM analysis, Multibody Syst. Dyn. 32 (1) (2014) 87–116, http://dx.doi.org/10.1007/s11044-013-9394-3.

[10] A.P. Deshmukh, J.T. Allison, Multidisciplinary dynamic optimization of horizontal axis wind turbine design, Struct. Multidiscip. Optim. 53 (1) (2016) 15–27, http://dx.doi.org/10.1007/s00158-015-1308-y.

[11] D.S. Zalkind, G.K. Ananda, M. Chetan, D.P. Martin, C.J. Bay, K.E. Johnson, E. Loth, D.T. Griffith, M.S. Selig, L.Y. Pao, System-level design studies for large rotors, Wind Energy Sci. 4 (4) (2019) 595–618, http://dx.doi.org/10.5194/wes-4-595-2019.

[12] P. Bortolotti, K. Dixon, E. Gaertner, M. Rotondo, G. Barter, An efficient approach to explore the solution space of a wind turbine rotor design process, J. Phys. Conf. Ser. 1618 (2020) 042016, http://dx.doi.org/10.1088/1742-6596/1618/4/042016.

[13] K. Malaawi, Structural Design Optimization of Wind Turbine Structure (Ph.D. thesis), Cairo University, Giza, Egypt, 1997, URL: https://www.researchgate.net/publication/261795912_Structural_Design_Optimization_of_Wind_Turbine_Structure/citations.

[14] H.M. Negm, K.Y. Maalawi, Structural design optimization of wind turbine towers, Comput. Struct. 74 (6) (2000) 649–666, http://dx.doi.org/10.1016/S0045-7949(99)00079-6.

[15] G. Horvath, L. Toth, New methods in wind turbine tower design, Wind Eng. 25 (3) (2001) 171–178, http://dx.doi.org/10.1260/0309524011495971.

[16] S. Yoshida, Wind turbine tower optimization method using a genetic algorithm, Wind Eng. 30 (6) (2006) 453–469, http://dx.doi.org/10.1260/030952406779994150.

[17] P.E. Uys, J. Farkas, K. Jármai, F. van Tonder, Optimisation of a steel tower for a wind turbine structure, Eng. Struct. 29 (7) (2007) 1337–1342, http://dx.doi.org/10.1016/j.engstruct.2006.08.011.

[18] S. Al-Sanad, L. Wang, J. Parol, A. Kolios, Reliability-based design optimisation framework for wind turbine towers, Renew. Energy 167 (2021) 942–953, http://dx.doi.org/10.1016/j.renene.2020.12.022.

[19] T. Ashuri, M.B. Zaaijer, J.R.R.A. Martins, G.J.W. van Bussel, G.A.M. van Kuik, Multidisciplinary design optimization of offshore wind turbines for minimum levelized cost of energy, Renew. Energy 68 (2014) 893–905, http://dx.doi.org/10.1016/j.renene.2014.02.045.

[20] J. Jonkman, S. Butterfield, W. Musial, G. Scott, Definition of a 5-MW Reference Wind Turbine for Offshore System Development, Technical Report, National Renewable Energy Laboratory (NREL), Golden, CO (United States), 2009.

[21] A.S. Ning, R. Damiani, P.J. Moriarty, Objectives and constraints for wind turbine optimization, J. Solar Energy Eng. 136 (4) (2014) 041010, http://dx.doi.org/10.1115/1.4027693.

[22] P. Bortolotti, C.L. Bottasso, A. Croce, Combined preliminary–detailed design of wind turbines, Wind Energy Sci. 1 (1) (2016) 71–88, http://dx.doi.org/10.5194/wes-1-71-2016.

[23] J. Zhu, Z. Zhou, X. Cai, Multi-objective aerodynamic and structural integrated optimization design of wind turbines at the system level through a coupled blade-tower model, Renew. Energy 150 (2020) 523–537, http://dx.doi.org/10.1016/j.renene.2020.01.013.

[24] J.G. Simpson, M. Kaminski, E. Loth, Influence of tower shadow on downwind flexible rotors: Field tests and simulations, Wind Energy 25 (5) (2022) 881–896, http://dx.doi.org/10.1002/we.2703.

[25] E. Loth, G. Ananda, M. Chetan, R. Damiani, D.T. Griffith, K. Johnson, S. Kianbakht, M. Kaminski, L. Pao, M. Phadnis, C.C. Qin, A. Scholbrock, M. Selig, J. Simpson, S. Yao, Field tests of a highly flexible downwind ultralight rotor to mimic a 13-MW turbine rotor, J. Phys. Conf. Ser. 2265 (3) (2022) 032031, http://dx.doi.org/10.1088/1742-6596/2265/3/032031.

[26] E. Frau, C. Kress, N. Chokani, R.S. Abhari, Comparison of performance and unsteady loads of multimegawatt downwind and upwind turbines, J. Solar Energy Eng. 137 (4) (2015) http://dx.doi.org/10.1115/1.4030314.

[27] A. Ning, D. Petch, Integrated design of downwind land-based wind turbines using analytic gradients, Wind Energy 19 (12) (2016) 2137–2152, http://dx.doi.org/10.1002/we.1972.

[28] S.M. Larwood, R. Chow, Comparison of upwind and downwind operation of the NREL Phase VI Experiment, J. Phys. Conf. Ser. 753 (2016) 022041, http://dx.doi.org/10.1088/1742-6596/753/2/022041.

[29] Z. Wang, W. Tian, H. Hu, A Comparative study on the aeromechanic performances of upwind and downwind horizontal-axis wind turbines, Energy Convers. Manage. 163 (2018) 100–110, http://dx.doi.org/10.1016/j.enconman.2018.02.038.

[30] P. Bortolotti, A. Kapila, C.L. Bottasso, Comparison between upwind and downwind designs of a 10 MW wind turbine rotor, Wind Energy Sci. 4 (1) (2019) 115–125, http://dx.doi.org/10.5194/wes-4-115-2019.
[31] P. Bortolotti, H. Ivanov, N. Johnson, G.E. Barter, P. Veers, N. Namura, Challenges, opportunities, and a research roadmap for downwind wind turbines, Wind Energy 25 (2) (2022) 354–367, http://dx.doi.org/10.1002/we.2676.
[32] E. Loth, M. Selig, P. Moriarty, Morphing segmented wind turbine concept, in: 28th AIAA Applied Aerodynamics Conference, in: Fluid Dynamics and Co-located Conferences, American Institute of Aeronautics and Astronautics, 2010, http://dx.doi.org/10.2514/6.2010-4400.
[33] C. Noyes, C. Qin, E. Loth, Analytic analysis of load alignment for coning extreme-scale rotors, Wind Energy 23 (2) (2020) 357–369, http://dx.doi.org/10.1002/we.2435.
[34] S. Yao, M. Chetan, D.T. Griffith, A.S. Escalera Mendoza, M.S. Selig, D. Martin, S. Kianbakht, K. Johnson, E. Loth, Aero-structural design and optimization of 50 MW wind turbine with over 250-m blades, Wind Eng. 46 (1) (2021) 273–295, http://dx.doi.org/10.1177/0309524X211027355.
[35] C.J. Bay, R. Damiani, L.J. Fingersh, S. Hughes, M. Chetan, S. Yao, D.T. Griffith, G.K. Ananda, M.S. Selig, D. Zalkind, L. Pao, D. Martin, K. Johnson, M. Kaminski, E. Loth, Design and testing of a scaled demonstrator turbine at the national wind technology center, in: AIAA Scitech 2019 Forum, American Institute of Aeronautics and Astronautics, San Diego, California (United States), 2019, p. 13, http://dx.doi.org/10.2514/6.2019-1068.
[36] M. Kaminski, C. Noyes, E. Loth, R. Damiani, S. Hughes, C. Bay, M. Chetan, D.T. Griffith, K. Johnson, D. Martin, Gravo-aeroelastic scaling of a 13-MW downwind rotor for 20% scale blades, Wind Energy 24 (3) (2020) 229–245, http://dx.doi.org/10.1002/we.2569.
[37] NREL, Standalone AeroDyn v15, National Renewable Energy Laboratory (NREL), 2017, URL: https://www.nrel.gov/wind/nwtc/aerodyn.html, accessed on February 6, 2023.
[38] J.M. Jonkman, G.J. Hayman, B.J. Jonkman, R.R. Damiani, R.E. Murray, AeroDyn V15 User's Guide and Theory Manual, Technical Report, National Renewable Energy Laboratory (NREL), Golden, Colorado, 2017, p. 46.
[39] M. Chetan, D.T. Griffith, S. Yao, Flutter predictions in the design of extreme-scale segmented ultralight morphing rotor blades, in: AIAA Scitech 2019 Forum, American Institute of Aeronautics and Astronautics, San Diego, California (United States), 2019, pp. 3–6, http://dx.doi.org/10.2514/6.2019-1298.
[40] M. Chetan, M.S. Sakib, D.T. Griffith, S. Yao, Aero-structural design study of extreme-scale segmented ultralight morphing rotor blades, in: AIAA Aviation 2019 Forum, American Institute of Aeronautics and Astronautics, Dallas, Texas (United States), 2019, p. 4, http://dx.doi.org/10.2514/6.2019-3347.
[41] A.S. Escalera Mendoza, M. Chetan, D.T. Griffith, Quantification of extreme-scale wind turbine performance parameters due to variations in beam properties, in: AIAA Scitech 2021 Forum, American Institute of Aeronautics and Astronautics, Virtual, 2021, pp. 4–6, http://dx.doi.org/10.2514/6.2021-1603.
[42] J. Berg, B. Resor, Numerical Manufacturing and Design Tool (NuMAD v2.0) for Wind Turbine Blades: User's Guide, Technical Report SAND2012-7028, Sandia National Laboratories (SNL), 2012, p. 72, http://dx.doi.org/10.2172/1051715.
[43] D.T. Griffith, T.D. Ashwill, The Sandia 100-Meter All-Glass Baseline Wind Turbine Blade: SNL100-00, Technical Report SAND2011-3779, Sandia National Laboratories (SNL), 2011.
[44] GL, IV – Rules and guideline industrial services, in: Guideline for the Certification of Wind Turbines, 2012 ed., Germanischer Lloyd, Hamburg, Germany, 2012, pp. 4.1–6.51.
[45] G.S. Bir, User's Guide to PreComp (Pre-Processor for Computing Composite Blade Properties), Technical Report NREL/TP-500-38929, National Renewable Energy Laboratory (NREL), Golden, Colorado (United States), 2006, http://dx.doi.org/10.2172/876556.
[46] MATLAB, version R2019a, The MathWorks Inc., 2019.
[47] R.D.F. Lopez, A 3D Finite Beam Element for the Modelling of Composite Wind Turbine Wings (Master's thesis), Royal Institute of Technology, Stockholm, Sweden, 2013.
[48] IEC, Part 1: Design requirements, in: IEC 61400-1 Wind Turbines, third ed., International Electrotechnical Comission (IEC), Geneva, Switzerland, 2005, pp. 34–36.
[49] M. Garcia-Sanz, A metric space with LCOE isolines for research guidance in wind and hydrokinetic energy systems, Wind Energy 23 (2) (2020) 291–311, http://dx.doi.org/10.1002/we.2429.
[50] NREL, Wind-Plant Integrated System Design and Engineering Model (WISDEM), National Renewable Energy Laboratory (NREL), 2019.
[51] B. Ennis, C. Kelley, B. Naughton, R. Norris, S. Das, D. Lee, D. Miller, Optimized Carbon Fiber Composites in Wind Turbine Blade Design, Technical Report SAND–2019-14173, Sandia National Laboratories (SNL), 2019, http://dx.doi.org/10.2172/1592956.
[52] T. Stehly, P. Duffy, 2020 Cost of Wind Energy Review, Technical Report NREL/TP-5000-81209, National Renewable Energy Laboratory (NREL), Golden, Colorado, 2021, http://dx.doi.org/10.2172/1838135.
[53] G.K. Ananda, S. Bansal, M.S. Selig, Aerodynamic design of the 13.2 MW SUMR-13i wind turbine rotor, in: 2018 Wind Energy Symposium, American Institute of Aeronautics and Astronautics, Kissimmee, Florida, 2018, http://dx.doi.org/10.2514/6.2018-0994.
[54] L.Y. Pao, K.E. Johnson, Control of wind turbines, IEEE Control Syst. Mag. 31 (2) (2011) 44–62.
[55] D.S. Zalkind, E. Dall'Anese, L.Y. Pao, Automatic controller tuning using a zeroth-order optimization algorithm, Wind Energy Sci. 5 (4) (2020) 1579–1600.
[56] NREL, OpenFAST v2.1.0, National Renewable Energy Laboratory (NREL), 2019, URL: https://openfast.readthedocs.io/en/main/, accessed on February 6, 2023.